Article

Cell Metabolism

Reducing Hypothalamic Stem Cell Senescence Protects against Aging-Associated Physiological Decline

Graphical Abstract

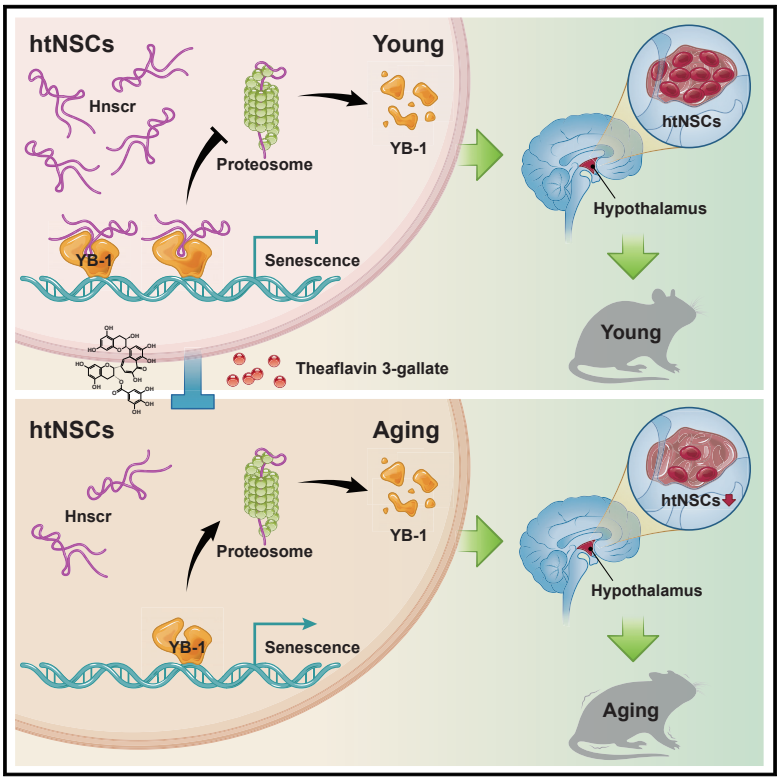

Highlights

- The lncRNA *Hnscr* is highly expressed in htNSCs of young mice but decreases during aging
- *Hnscr* depletion promotes the senescence of htNSCs and aging-like phenotypes
- *Hnscr* attenuates htNSC senescence by binding to YB-1 to prevent its degradation
- Theaflavin 3-gallate mimics *Hnscr* and ameliorates aging-related physiological disorders

Authors

Yu-Zhong Xiao, Mi Yang, Ye Xiao, ..., Chang-Jun Li, Dongsheng Cai, Xiang-Hang Luo

Correspondence

xianghangluo@sina.com (X.-H.L.), dongsheng.cai@einstein.yu.edu (D.C.)

In Brief

Loss of *Hnscr* is important for the senescence of hypothalamic stem cells via allowing YB-1 degradation and thus contributes to aging-related physiological decline.

Xiao et al., 2020, Cell Metabolism *31*, 1–15
March 3, 2020
https://doi.org/10.1016/j.cmet.2020.01.002

CellPress

Please cite this article in press as: Xiao et al., Reducing Hypothalamic Stem Cell Senescence Protects against Aging-Associated Physiological Decline, Cell Metabolism (2020), https://doi.org/10.1016/j.cmet.2020.01.002

Cell Metabolism
Article

Reducing Hypothalamic Stem Cell Senescence Protects against Aging-Associated Physiological Decline

Yu-Zhong Xiao,[1,4] Mi Yang,[1,3,4] Ye Xiao,[1,4] Qi Guo,[1,3] Yan Huang,[1] Chang-Jun Li,[1] Dongsheng Cai,[2,*] and Xiang-Hang Luo[1,5,*]

[1]Department of Endocrinology, Endocrinology Research Center, Xiangya Hospital of Central South University, Changsha, Hunan 410008, China
[2]Department of Molecular Pharmacology, Albert Einstein College of Medicine, Bronx, NY 10461, USA
[3]Key Laboratory of Organ Injury, Aging and Regenerative Medicine of Hunan Province, Changsha, Hunan 410008, China
[4]These authors contributed equally
[5]Lead Contact
*Correspondence: xianghangluo@sina.com (X.-H.L.), dongsheng.cai@einstein.yu.edu (D.C.)
https://doi.org/10.1016/j.cmet.2020.01.002

SUMMARY

Age-dependent loss of hypothalamic neural stem cells (htNSCs) is important for the pathological consequences of aging; however, it is unclear what drives the senescence of htNSCs. Here, we report that a long non-coding RNA, *Hnscr*, is abundantly expressed in the htNSCs of young mice but decreases markedly in middle-aged mice. We show that depletion of *Hnscr* is sufficient to drive the senescence of htNSCs and aging-like phenotypes in mice. Mechanistically, *Hnscr* binds to Y-box protein 1 (YB-1) to prevent its degradation and thus the attenuation of transcription of the senescence marker gene $p16^{INK4A}$. Through molecular docking, we discovered that a naturally occurring small compound, theaflavin 3-gallate, can mimic the activity of *Hnscr*. Treatment of middle-aged mice with theaflavin 3-gallate reduced the senescence of htNSCs while improving aging-associated pathology. These results point to a mediator of the aging process and one that can be pharmacologically targeted to improve aging-related outcomes.

INTRODUCTION

The hypothalamus, which has crucial functions in neuroendocrine regulation, communicates with peripheral tissues and responds to environmental and nutritional cues to modulate various aspects of physiological functions. Recently, it was discovered that the hypothalamus plays critical roles in supervising the process of aging (Zhang et al., 2013; Zhang et al., 2017), and hypothalamic neural stem/progenitor cells (htNSCs) mediate this process (Zhang et al., 2017). These cells exist in the hypothalamic third-ventricle wall and mediobasal hypothalamic (MBH) parenchyma (Li et al., 2012) and undergo age-dependent loss, becoming almost entirely absent in advanced aging (Zhang et al., 2017). It is critical to understand the mechanisms that govern the loss of htNSCs to develop strategies to potentially improve the outcomes of comorbidities that are associated with aging. Here, we identified a long noncoding RNA (lncRNA), *Hnscr*, that is abundantly present in the htNSCs of young mice but is substantially diminished in the htNSCs of middle-aged mice.

Long non-coding RNAs (LncRNAs) are classified as transcripts longer than 200 nucleotides that have limited potential to encode proteins (Akerman et al., 2017; Knoll et al., 2015; Zhao et al., 2014). LncRNAs regulate the expression of target genes at the transcriptional level (Arab et al., 2014), post-transcriptional level (Guo et al., 2016), and post-translational level (Liu et al., 2015) by binding with DNA, RNA, or protein complexes or by serving as the precursors of miRNAs (Lu et al., 2017). LncRNAs regulate a wide range of biological processes via diverse mechanisms (Guttman and Rinn, 2012; Ransohoff et al., 2018; Wong et al., 2018). Thus, stemming from our screening information, we investigated the relationship between *Hnscr* and htNSCs, revealing that senescence of these cells is

Context and Significance

Understanding the mechanisms of aging is important for developing strategies to combat the many chronic comorbidities associated with it. One of the causes of aging is the exhaustion of stem cells, including hypothalamic neural stem cells (htNSCs), because of their senescence. Here, Xiang-Hang Luo and colleagues investigate the role of a long non-coding RNA, termed *Hnscr*, which is highly expressed in htNSCs but decreases markedly with age. They found that *Hnscr* depletion is sufficient to cause senescence of these stem cells and aging-like phenotypes in mice. They also identified a natural small compound, theaflavin 3-gallate, which a key component of black tea, that mimics the action of *Hnscr*, and its use in mice greatly reduced the senescence of htNSCs while preventing aging-related physiological disorders.

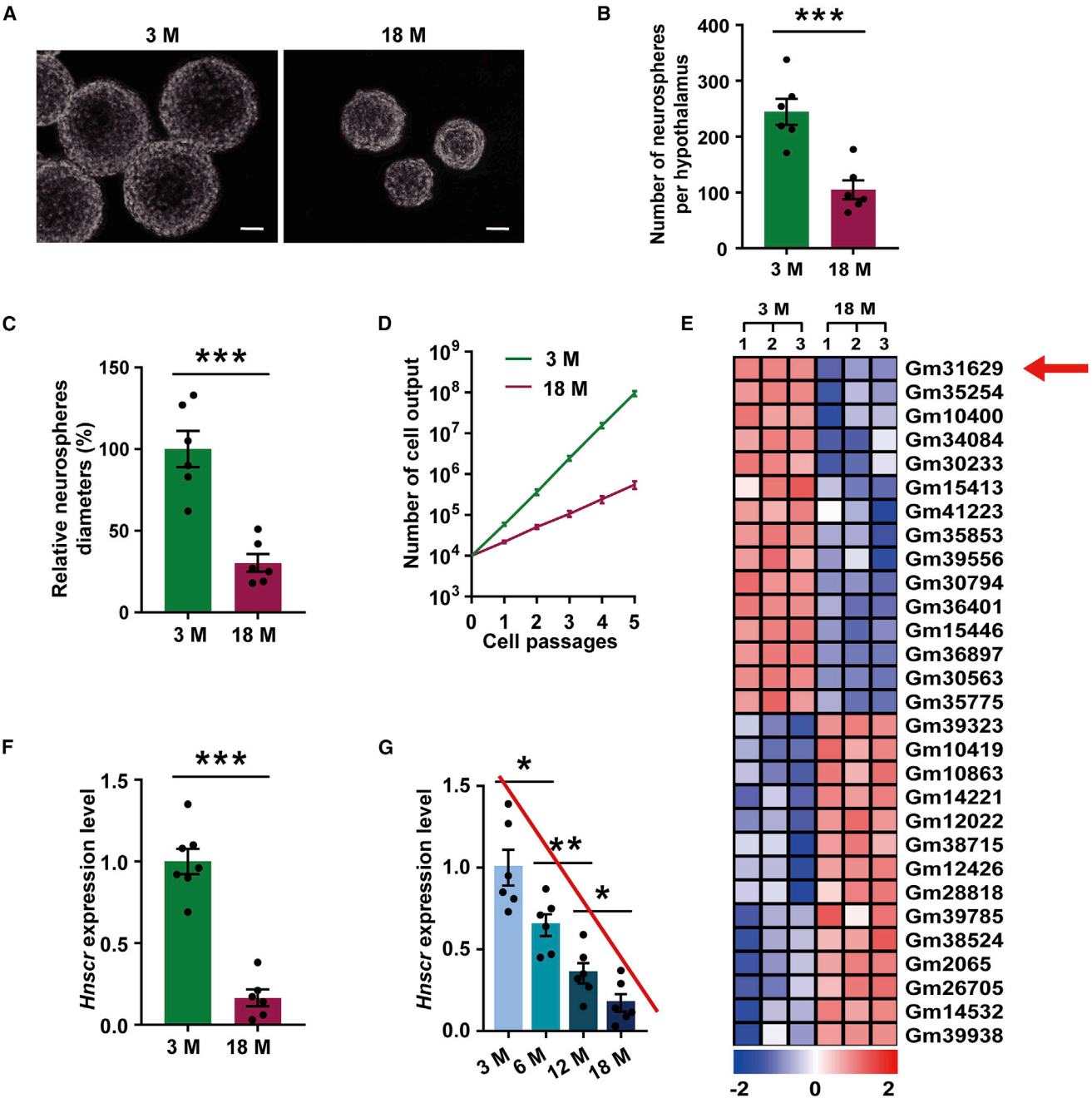

Figure 1. Expression of *Hnscr* Decreases in htNSCs of Mice during Aging

(A–D) Representative images (n = 18 photographs from 3 experiments) of neurospheres generated from the hypothalami of young mice (3 months old) and middle-aged mice (18 months old) (A). Scale bars, 100 μm. Their quantitation is shown in (B); relative size in (C); and cell output over 5 passages in (D).

(E) Heatmap of RNA-seq profiling of lncRNA expression in htNSCs from young mice (3 months) and middle-aged mice (18 months). Fold change > 2.5, false-discovery rate < 0.20.

(F) Relative *Hnscr* expression in htNSCs from 3-month-old and 18-month-old mice as determined by qRT-PCR. The value of the expression in the 3-month-old mice was set at an arbitrary value = 1.

(G) Age-associated changes of *Hnscr* expression in the htNSCs of WT mice. The value of the expression in the 3-month-old mice was set at an arbitrary value = 1.

Data are shown as mean ± SEM, (n = 6–7 in [A]–[D] and [F]–[G]; n = 3 in [E]). *p < 0.05; **p < 0.01; ***p < 0.001 by two-tailed Student's t test or one-way ANOVA.

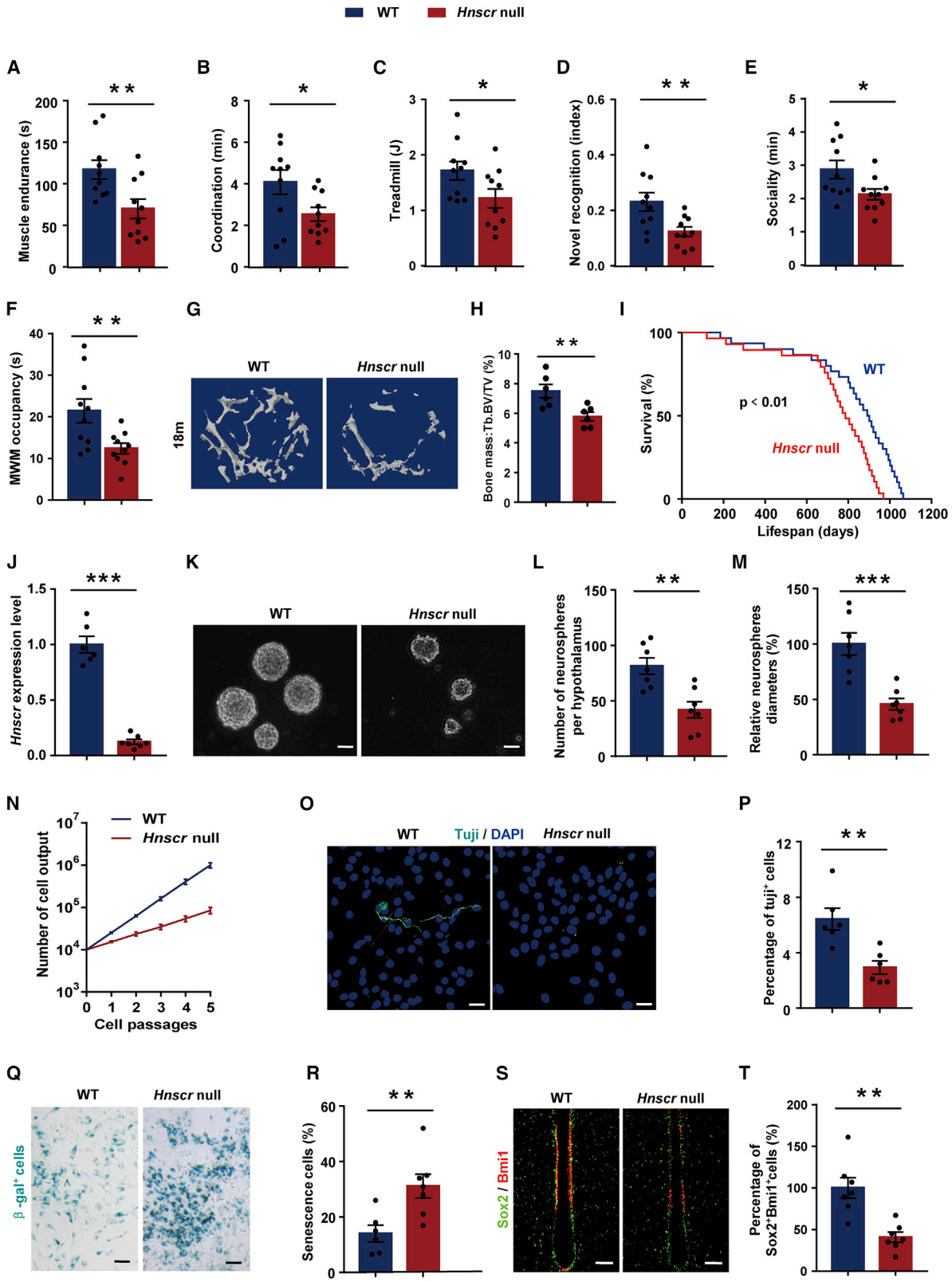

(legend on next page)

controlled by this lncRNA, and, thus, loss of *Hnscr* contributes to aging-associated pathologies.

RESULTS

Hnscr Levels Decrease in htNSCs of Mice during Aging

To assess the different characteristics of htNSCs from young and middle-aged mice, we analyzed hypothalamic tissue from 3- and 18-month-old C57BL/6J mice for neurosphere formation (Li et al., 2012; Zhang et al., 2017). Neurospheres derived from the hypothalamus of middle-aged mice were much fewer, smaller, and poorly grown than those derived from young mice (Figures 1A–1D). Given the important roles of lncRNAs in regulating many aspects of cell biology, including survival, we were interested in exploring the patterns of lncRNAs in these cells under different age conditions. Indeed, htNSCs abundantly contain miRNAs and RNAs of larger sizes (Zhang et al., 2017). We performed RNA sequencing to identify differences in lncRNAs between htNSCs derived from young mice versus those derived from aged mice (Figure 1E). A total of 1,122 differentially expressed lncRNAs with at least a 2.5-fold change were identified. We selected 5 lncRNAs with the following properties: (1) showed high expression in htNSCs that strikingly decreased during aging; (2) showed homology and conservation between human and mice; and (3) had no splicing or overlap with any coding genes present in the National Center for Biotechnology Information's RefSeq database, University of California Santa Cruz Genome Browser, or Ensembl genome browser annotations. Among these differentially expressed lncRNAs, *Gm31629* showed the best evolutionary conservation, which had several orthologous genomic regions of greater than 200 base pairs (bp) and showed similar locations in the genome between human and mice, and therefore was selected for further study.

The decreased expression of *Gm31629* in the htNSCs of aged mice was further confirmed by quantitative real-time PCR analysis (Figure 1F). We measured the expression pattern of *Gm31629* in the cerebral cortex, hypothalamus, htNSCs, liver, muscle, white adipose tissue, brown adipose tissue, kidney, and heart, finding that *Gm31629* expression was particularly high in htNSCs and the hypothalamus (Figure S1). We thus referred to *Gm31629* as *Hnscr*, given that it is htNSC-related. In addition, we found that the levels of *Hnscr* were consistently negatively correlated with increasing age (Figure 1G).

Depletion of *Hnscr* induces aging-like phenotypes

These above data led us to explore whether *Hnscr* might play an important role in the loss of htNSCs and the aging process. To evaluate whether *Hnscr* could be physiologically relevant to aging, we generated *Hnscr* null mice via gene targeting with the TetraOne technique. When young, the *Hnscr* null mice and their littermate controls were indistinguishable; for example, they were similar in body weight (Figure S2A) and in physiology, such as in behavior and reproductive fitness (Figures S2B–S2K). Then, we followed up the effects of *Hnscr* knockout on whole-body physiology in middle-aged mice through behavioral analyses. *Hnscr* null mice exhibited lower muscle endurance performance, coordination, treadmill running, novel object recognition, and sociality function (Figures 2A–2E). Further, Morris water-maze analyses demonstrated that the *Hnscr* null mice had a larger decline in cognitive ability than the control mice had (Figure 2F).

Metabolically, glucose-tolerance tests (GTTs) and insulin-tolerance tests (ITTs) showed that *Hnscr* null mice had impaired glucose tolerance (Figure S3A), although insulin resistance was similar between the null mice and controls (Figure S3B). Reproductive fitness was also examined, showing that the weight of testis and sperm count and sperm motility of *Hnscr* null mice were lower than those of the controls (Figures S3C–S3E). Micro-computed tomography (CT) analysis showed that aging-related bone-mass loss was more evident in the *Hnscr* null mice than in the controls (Figures 2G and 2H). Consistent with all these observations, the lifespan of *Hnscr* null mice decreased significantly in comparison with wild-type control mice (Figure 2I), further supporting the observation that *Hnscr* null mice developed an aging-like phenotype.

Depletion of *Hnscr* Promotes htNSC Senescence at Middle Age

In the meanwhile, we analyzed the ability to derive neurospheres from the hypothalami of *Hnscr* null mice. The neurospheres from middle-aged *Hnscr* null mice were much fewer and smaller, whereas htNSCs in these neurospheres were poorer in both proliferation and differentiation compared with age-matched

Figure 2. *Hnscr* Knockout Increases the Senescence of htNSCs and Aging

(A–F) The physiological changes including muscle endurance performance (A), coordination (B), treadmill running (C), novel object recognition (D), and sociality function (E) of 18-month-old *Hnscr* null mice and littermate WT mice.

(G and H) Representative micro-CT images (n = 12 photographs from 2 experiments) (G) and quantitative analysis (H) of femur of 18-month-old *Hnscr* null mice and littermate WT mice. Tb. BV/TV, trabecular bone volume per tissue volume.

(I) Lifespan of *Hnscr* null mice and littermate WT mice.

(J) Relative *Hnscr* expression in htNSCs of 18-month-old *Hnscr* null mice and littermate WT mice. The value of the expression in the WT mice was set at an arbitrary value = 1.

(K–N) Representative images (n = 21 photographs from 3 experiments) of neurospheres generated from the hypothalami of 18-month-old *Hnscr* null mice and littermate WT mice (K). Scale bar, 100 μm. Their quantitation is shown in (L); relative size in (M); and the cell output over 5 passages in (N).

(O and P) Representative images (n = 18 photographs from 3 experiments) of Tuj1 immunostaining of dissociated htNSCs from 18-month-old *Hnscr* null mice and littermate WT mice (O). Scale bar, 100 μm. The percentage of $Tuj1^+$ cells is shown in (P).

(Q and R) Representative images (n = 21 photographs from 3 experiments) of SA-βGal staining of dissociated htNSCs from 18-month-old *Hnscr* null mice and littermate WT mice (Q). Scale bar, 100 μm. The percentage of senescent cells is shown in (R).

(S and T) Representative images (n = 14 photographs from 2 experiments) of hypothalamic sections of 18-month-old *Hnscr* null mice and littermate WT mice co-stained with SOX2 and BMI1 (S). Scale bar, 100 μm. The relative percentage of $SOX2^+BMI1^+$ cells is shown in (T).

Data are shown as mean ± SEM, (n = 10 in [A]–[F], n = 29–30 in [I], and n = 6–7 in [G]–[H] and [J]–[T]). *$p < 0.05$; **$p < 0.01$; ***$p < 0.001$ by two-tailed Student's t test or one-way ANOVA. Lifespan analysis was performed by Kaplan–Meier survival analysis.

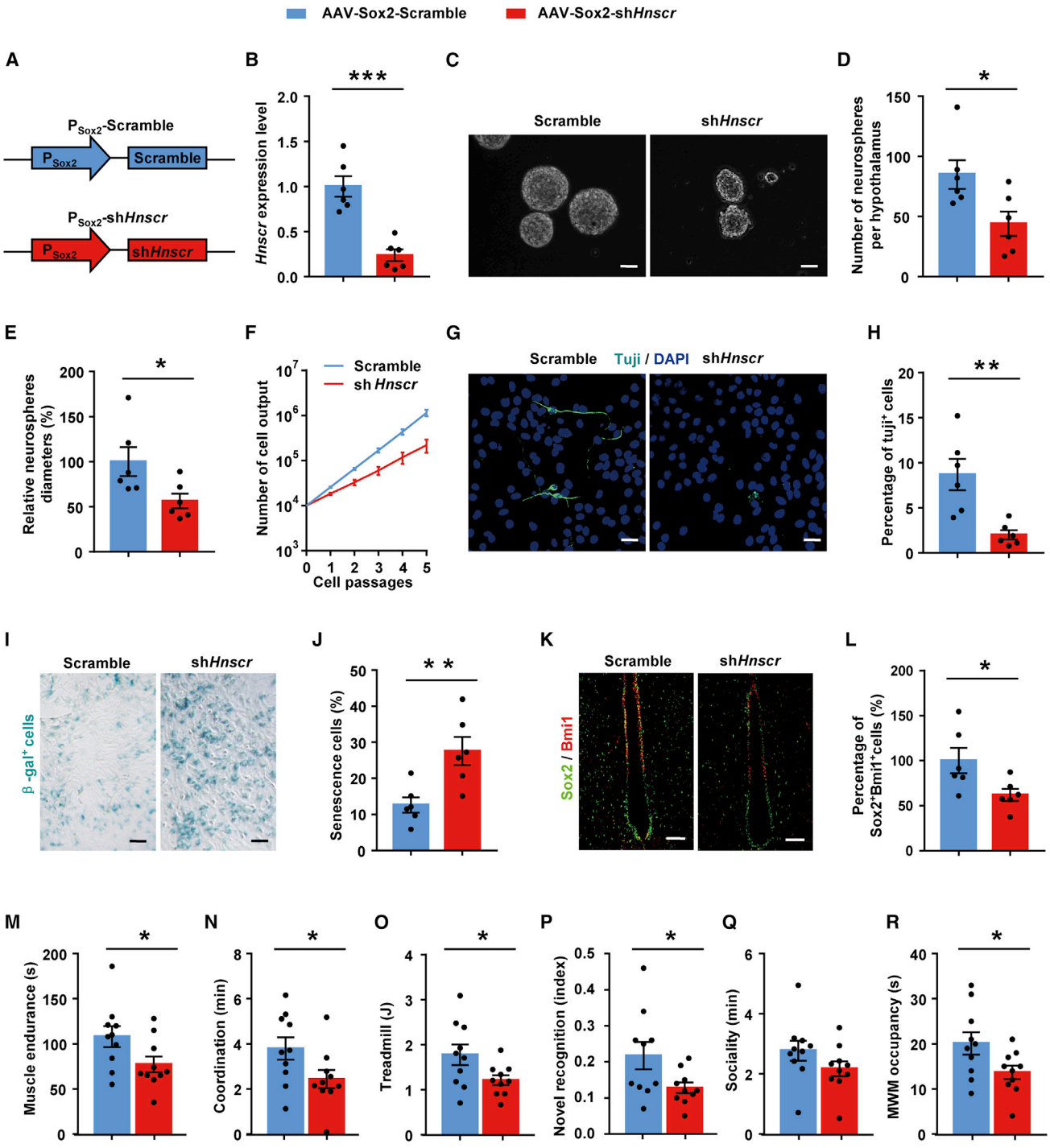

Figure 3. Local *Hnscr* Knockdown Enhances htNSC Senescence and Aging

(A) Schematic of adeno-associated viral vector that expressed shRNAs targets for *Hnscr* and the control-vector-expressing scramble RNAs under the control of Sox2 promoter (AAV-Sox2-sh*Hnscr* and AAV-Sox2-Scramble).

(B) The levels of *Hnscr* in htNSCs of WT mice that underwent AAV-Sox2-sh*Hnscr* and AAV-Sox2-Scramble treatment. The value of the expression in the control-vector injection mice was set at an arbitrary value = 1.

(C–F) Representative images (n = 18 photographs from 3 experiments) of neurospheres generated from mice 1 month after viral injection (C). Scale bar, 100 μm. Their quantitation is shown in (D); relative size in (E); and the cell output over 5 passages in (F).

(G and H) Representative images (n = 18 photographs from 3 experiments) of Tuj1 immunostaining of dissociated htNSCs from AAV-injected mice (G). Scale bar, 100 μm. The percentage of Tuj1$^+$ cells is seen in (H).

(legend continued on next page)

controls (Figures 2J–2P). Senescence-associated β-galactosidase (SA-βGal) staining further revealed that the percentage of senescent cells were higher in htNSCs derived from *Hnscr* null mice at middle age than in htNSCs from age-matched control mice (Figures 2Q and 2R). Consistently, *Hnscr* null mice displayed an accelerated rate of age-dependent loss of htNSCs compared to the control mice (Figures 2S and 2T). We also examined the number of neurons in the MBH and subtypes, including pro-opiomelanocortin (POMC) neurons and neuropeptide Y (NPY) neurons, but did not find a major difference between *Hnscr* null mice and control mice (Figures S3F–S3I). This result agreed with our observation that loss of *Hnscr* had minimal effects when animals were young, because the function of these cells for hypothalamic neurogenesis is more relevant to the developmental stage and young condition rather than aged condition. Taken together, loss of *Hnscr* leads to an induction of htNSC senescence during middle age.

Depletion of *Hnscr* in htNSCs Leads to Senescence and Aging-like Disorders

To more directly explore the role of *Hnscr* in affecting htNSCs senescence *in vivo*, we generated a mouse model with *Hnscr* specifically depleted in htNSCs. The 14-month-old wild-type (WT) mice were obtained by bilaterally intra-MBH injection of *Sox2* promoter-driven adeno-associated viruses (AAVs) expressing microRNA miR30-based short hairpin RNAs (shRNAs) that target *Hnscr* (AAV-Sox2-sh*Hnscr*), as illustrated in Figure 3A. One month later, the hypothalamic tissue of mice was isolated for neurosphere culture. Quantitative real-time reverse transcription PCR (qRT-PCR) analysis confirmed that the expression of *Hnscr* was largely abrogated in the htNSCs of mice injected with AAV-Sox2-sh*Hnscr* (Figure 3B). Based on neurosphere assays, cell-proliferation-rate analysis, cell-differentiation assays, and SA-βGal staining, htNSCs derived from AAV-Sox2-sh*Hnscr*-injected mice were more prone to senescence than those derived from the control mice (Figures 3C–3J). Consistent with the senescence, the number of htNSCs were lower in the hypothalamus of AAV-Sox2-sh*Hnscr*-injected mice than those in the control mice (Figures 3K and 3L). Four months after injection of the AAVs, these mice were subjected to various physiological and histological analyses that collectively indicate aging; to summarize, the AAV-Sox2-sh*Hnscr*-injected mice exhibited impaired muscle functions, cognition, sociality, metabolism, and reproductive fitness (Figures 3M–3R and S4A–S4E), although these phenotypes were generally weaker than whole-body knockout of *Hnscr* presented in Figure 2. Injection of AAV-Sox2-sh*Hnscr* did not affect the number of hypothalamic neurons (Figures S4F–S4I). Taken together, these results suggest that disruption of *Hnscr* expression promotes the senescence of htNSCs and contribute to accelerated aging-related physiological decline in mice.

Hnscr Directly Interacts with Y-box Protein 1 (YB-1)

To explore the mechanism by which *Hnscr* regulates htNSC senescence, we performed RNA pull-down assays to identify proteins that interact with *Hnscr*. Among the identified *Hnscr*-associated proteins, Y-box protein 1 (YB-1) had the highest abundance (Figure 4A and Table S1). Our interest in this protein was piqued by a previous report that fibroblasts derived from YB-1-depleted embryos undergo premature senescence (Lu et al., 2005). To verify this target, we repeated the RNA pull-down assay and subjected the RNA pull-down proteins to western blotting with anti-YB-1 antibodies, detecting a strong signal among the proteins pulled down by the *Hnscr* RNA but not in the samples processed with antisense *Hnscr* or the other controls (Figure 4B). Only the full-length YB-1 protein (relative molecular weight ~50 kDa) was detected in the RNA pull-down assay (Figure 4B). Further, we performed RNA immunoprecipitation (RIP) in htNSCs to confirm the binding of YB-1 to *Hnscr* and found that the anti-YB-1 antibodies pulled down *Hnscr* (Figure 4C). For comparison, we assessed DbpA, a YB-1-interacting protein encoded by YBOX3, which showed a high value of peptide spectrum matches among the *Hnscr*-associated proteins (Table S1). Compared to use of a YB-1 antibody, the DbpA antibody led to a fractional pull-down of *Hnscr* (Figure S5A). To investigate which region of the *Hnscr* transcript could bind to YB-1, we generated a series of deletion mutants of *Hnscr*, which were transcribed and biotinylated for RNA pull-down assays. The deletion mutants that retained nucleotides 1–300 was found to bind to YB-1 almost as well as full-length *Hnscr* did. By contrast, the deletion mutants lacking nucleotides 1–300 did not interact with YB-1 (Figure 4D), suggesting that nucleotides 1–300 of *Hnscr* are necessary for its binding to YB-1. Next, to determine which domain of YB-1 binds to *Hnscr*, we generated a series of YB-1 truncations according to previous publications (Jürchott et al., 2003; Kloks et al., 2002; van Roeyen et al., 2013) (Figure S5C). Then, we transfected these YB-1 truncations into HEK293T cells and performed RNA pull-down assays. The results showed that deletion of the N terminus of YB-1 abolished the interaction between *Hnscr* and YB-1 (Figures S5C and S5D), suggesting the N terminus is crucial for YB-1 binding to *Hnscr*.

Hnscr Regulates YB-1 via Protein Stability

Next, we investigated the interaction of *Hnscr* and YB-1 in htNSCs. Notably, the interaction did not occur at the transcriptional level, because *Hnscr* knockdown did not change the mRNA levels of YB-1, and YB-1 knockdown also did not affect the expression of *Hnscr* (Figures 4E and 4F). However, *Hnscr* knockdown significantly decreased the protein level of YB-1 (Figure 4G). For comparison, *Hnscr* knockdown did not affect the protein level of DbpA in htNSCs (Figure S5B). In parallel, we did an overexpression experiment showing that the protein

(I and J) Representative images (n = 18 photographs from 3 experiments) of SA-βGal staining of dissociated htNSCs from mice 1 month after viral injection (I). Scale bar, 100 μm. The percentage of senescent cells is shown in (J).

(K and L) Representative images (n = 12 photographs from 2 experiments) of SOX2 and BMI1 co-staining of hypothalamic sections of mice (K). Scale bar, 100 μm. The relative percentage of $SOX2^{+}BMI1^{+}$ cells is shown in (L).

(M–R) The physiological changes including muscle endurance performance (M), coordination (N), treadmill running (O), novel object recognition (P), sociality function (Q), and Morris-Water-Maze tests (R) of mice that underwent AAV-Sox2-sh*Hnscr* and AAV-Sox2-Scramble treatment.

Data are shown as mean ± SEM, (n = 6–7 in [B]–[L], n = 10 in [M]–[R]). *p < 0.05; **p < 0.01; ***p < 0.001 by two-tailed Student's t test or one-way ANOVA.

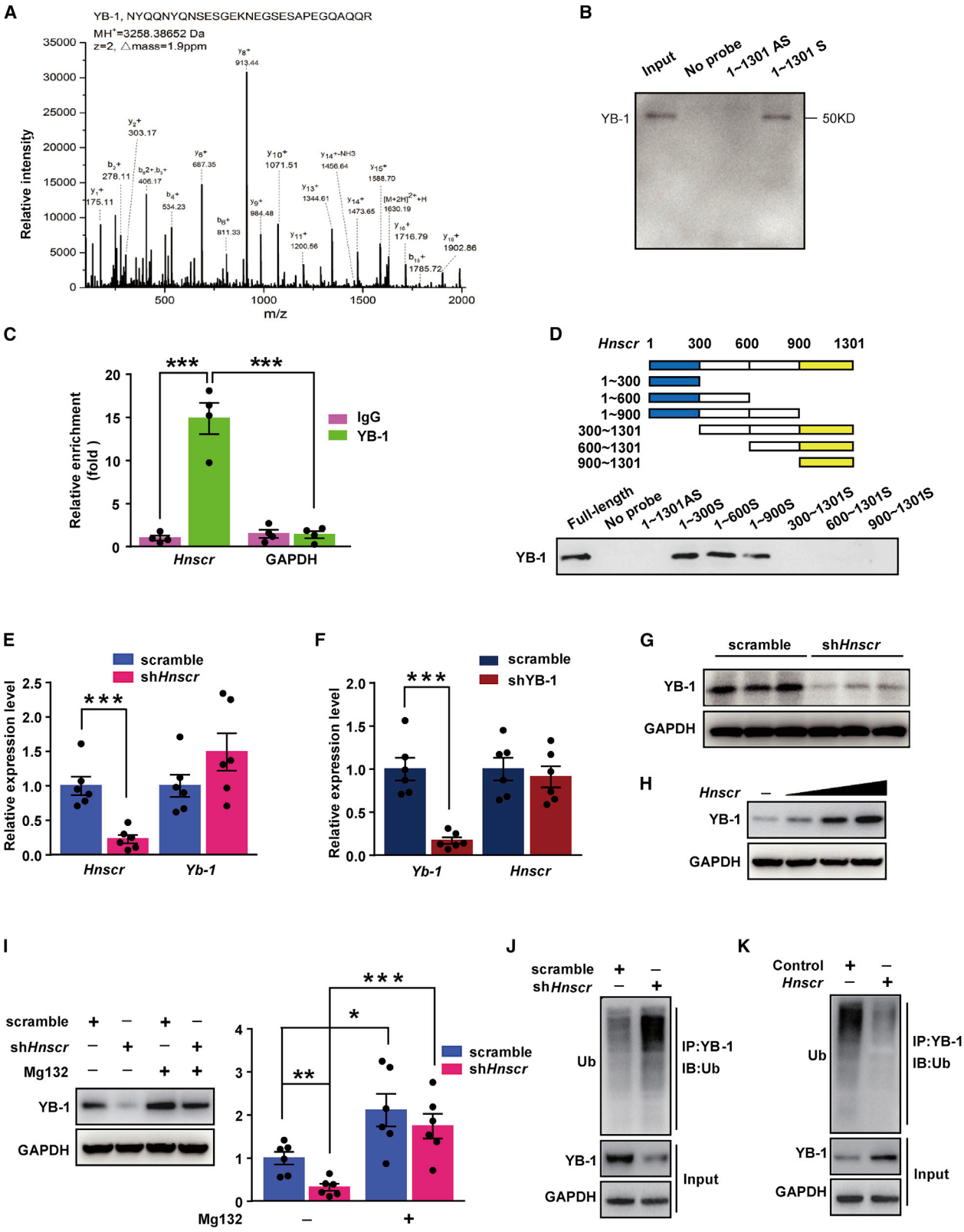

Figure 4. *Hnscr* Binds to YB-1 and Protects It from Degradation

(A) Mass spectrometry identified YB-1 in proteins pulled-down by biotinylated *Hnscr* in htNSCs.

(B) Biotinylated *Hnscr* retrieved YB-1 in htNSCs as detected by western blot.

(legend continued on next page)

level of YB-1 increased as *Hnscr* increased in a graded manner (Figure 4H). These results suggest that the *Hnscr*–YB-1 interaction might help stabilize YB-1 protein. When protein synthesis was inhibited, it was clear that *Hnscr* knockdown accelerated the degradation of YB-1 (Figure S5E), and *Hnscr* overexpression increased the half-life of the YB-1 protein (Figure S5F). Also, when cells were treated with the proteasome inhibitor Mg132, the protein level of YB-1 increased significantly (Figure 4I), suggesting the involvement of proteasome-mediated protein degradation. Furthermore, *Hnscr* knockdown significantly decreased the protein level of YB-1, and Mg132 treatment largely rescued this decrease (Figure 4I), supporting the hypothesis that *Hnscr* knockdown accelerated the proteasome-dependent degradation of YB-1.

Because YB-1 was previously shown to be degraded through ubiquitination (Dong et al., 2015), we further examined whether *Hnscr* could affect YB-1 ubiquitination. Indeed, higher levels of YB-1 ubiquitination were observed in htNSCs with *Hnscr* knockdown (Figure 4J), whereas *Hnscr* overexpression significantly decreased the ubiquitination levels of YB-1 (Figure 4K). Taken together, these results suggest that *Hnscr* stabilizes YB-1 by controlling its ubiquitination.

Hnscr Attenuates the Expression of $p16^{INK4A}$ by Stabilizing YB-1

To explore the downstream signaling of the *Hnscr*–YB-1 pathway in the regulation of htNSC senescence, we conducted RNA sequencing in htNSCs derived from *Hnscr* null mice and littermate WT mice. A total of 2,276 genes showed differential expression in *Hnscr* null htNSCs. We then performed gene-ontology (GO) analysis of the differentially expressed genes to explore the functional processes that are affected by *Hnscr* deficiency. The most significantly altered biological processes included signal pathways involved in cell senescence and apoptosis, inflammatory responses, glucose metabolism, and protein degradation (Figure S5G and Table S2). In these differentially expressed genes, we paid attention to $p16^{INK4A}$ (cyclin-dependent kinase 2a [CDKN2A]), a marker of cell senescence and cell-cycle arrest, because it was significantly upregulated in htNSCs with *Hnscr* deficiency (Figure S5H). The increase in the expression of $p16^{INK4A}$ was confirmed by qRT-PCR analysis (Figure 5A). In htNSCs with YB-1 knockdown, the mRNA of $p16^{INK4A}$ also increased (Figure 5B). Conversely, overexpression of YB-1 in *Hnscr*-deficient htNSCs rescued the decreased expression level of YB-1 and decreased the mRNA and protein levels of $p16^{INK4A}$ (Figures 5C and 5D). Knockdown of *Hnscr* or YB-1 in htNSCs both reduced the occupancy of YB-1 on the promoter region of $p16^{INK4A}$ (Figure S5I). Taken together, these results suggested that *Hnscr* attenuates the expression of $p16^{INK4A}$ via stabilizing YB-1, a possible mechanism for this lncRNA in suppressing the senescence of htNSCs.

Overexpression of YB-1 Rescues htNSC Senescence

Given that *Hnscr* inhibits the expression of $p16^{INK4A}$ via stabilizing YB-1, we then tested whether overexpression of YB-1 could rescue the increased senescence of *Hnscr*-depleted htNSCs. Adeno-associated viruses with *Sox2* promoter-driven overexpression of YB-1 (AAV-Sox2-YB-1) were bilaterally injected together with AAV-Sox2-sh*Hnscr* into the MBH of 14-month-old WT mice. One month after injection of the AAVs, the hypothalamic tissues of mice were isolated for neurosphere culture. qRT-PCR analysis confirmed that the mRNA levels of YB-1 increased and the expression levels of *Hnscr* decreased in htNSCs derived from mice injected with AAV-Sox2-YB-1 together with AAV-Sox2-sh*Hnscr* (Figure 5E). The *in vitro* neurosphere assay revealed that YB-1 overexpression significantly attenuated the effects of sh*Hnscr* in reducing the number and size of hypothalamic neurospheres (Figures 5F–5H). The *in vitro* cell-senescence assays indicated that increased levels of senescence in htNSCs derived from AAV-Sox2-sh*Hnscr*-injected mice were also significantly rescued by YB-1 overexpression (Figures 5I and 5J). Cell-proliferation-rate analysis showed that decreases in cell proliferation of *Hnscr*-depleted htNSCs were rescued by YB-1 overexpression (Figure 5K). Consistently, *in vivo* assays showed that YB-1 overexpression partially rescued the decreased number of htNSCs in the hypothalamus of *Hnscr*-depleted mice (Figure 5L). Hence, overexpression of YB-1 can help reduce the levels of senescence in *Hnscr*-depleted htNSCs.

Theaflavin 3-Gallate (TF2A) Acts as a Mimic of *Hnscr*

According to the findings above, we reasoned that enhancing the stability of YB-1 could be a strategy to alleviate htNSC senescence, leading to an amelioration of aging-related disorders in mice. Through searching the RCSB PDB database (http://www.rcsb.org/), we found that the three-dimensional structure of the human YB-1 protein (PDB code: 1H95) has been determined with nuclear magnetic resonance (NMR), but the structure of mouse YB-1 protein is still unknown, though it is known that the homology between human and mouse YB-1 protein is 97%

(C) YB-1-retrieved *Hnscr* RNA as detected by qRT-PCR analysis. The expression level of IgG-retrieved *Hnscr* was set at an arbitrary value = 1.
(D) Truncation mapping of YB-1 binding domain in *Hnscr*, the schematic diagram of full-length and truncated fragments of *Hnscr*, and western blot of YB-1 in samples pulled-down by different *Hnscr* fragments.
(E) qRT-PCR analysis of the expression of *Hnscr* and YB-1 in htNSCs expressing shRNAs targeting for *Hnscr* or scramble controls. The value of the expression in the scramble-treated htNSCs was set at an arbitrary value = 1.
(F) qRT-PCR analysis of the expression of *Hnscr* and YB-1 in htNSCs expressing shRNAs targeting for YB-1or scramble controls. The value of the expression in the scramble-treated htNSCs was set at an arbitrary value = 1.
(G) The protein level of YB-1 in htNSCs expressing shRNAs targeting for *Hnscr*.
(H) The protein levels of YB-1 in htNSCs with lentiviral vector-driven *Hnscr* overexpressed in a gradient.
(I) The protein levels of YB-1 in control and lentiviral vector-driven *Hnscr* knockdown htNSCs treated with vehicle or Mg132 as indicated. Left, representative images of western blot; right, quantification analysis of YB-1 in relation to glyceraldehyde 3-phosphate dehydrogenase (GAPDH).
(J and K) Western blot analysis of YB-1-associated ubiquitination in control and *Hnscr* knockdown htNSCs (J) or in control and *Hnscr* overexpression htNSCs (K) treated with Mg132.
Data are shown as mean ± SEM. The cell experiments were repeated 3 times. *$p < 0.05$; **$p < 0.01$; ***$p < 0.001$ by two-tailed Student's t test or two-way ANOVA.

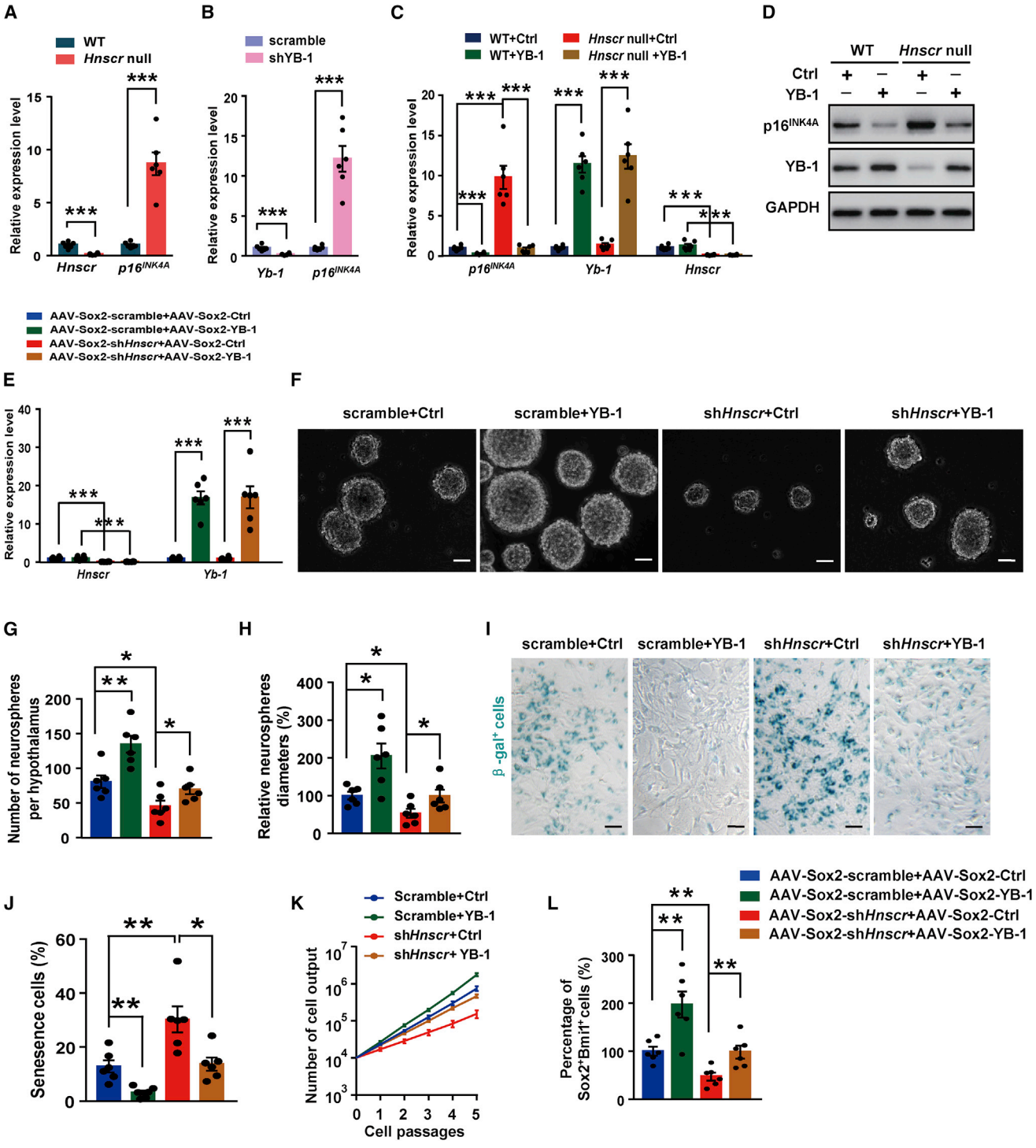

Figure 5. Overexpression of YB-1 Reduces the Senescent Effect of *Hnscr* Loss

(A) The mRNA levels of *Hnscr* and $p16^{INK4A}$ in htNSCs. The value of the expression in the WT mice was set at an arbitrary value = 1.

(B) The mRNA levels of *YB-1* and $p16^{INK4A}$ in htNSCs. The value of the expression in the scramble-treated htNSCs was set at an arbitrary value = 1.

(C) The mRNA levels of $p16^{INK4A}$ and *Yb-1* in htNSCs. The value of the expression in the WT mice without YB-1 overexpression was set at an arbitrary value = 1.

(D) $p16^{INK4A}$ and YB-1 protein levels in *Hnscr*-deleted or WT htNSCs with or without YB-1 overexpressed.

(E) The levels of *Hnscr* and *Yb-1* in htNSCs of WT mice 1 month after viral injection. The value of the expression in the control vector injection mice was set at an arbitrary value = 1.

(F–H) Representative images (n = 18 photographs from 3 of experiments) of neurospheres generated from mice 1 month after viral injection (F). Scale bar, 100 μm. Their quantitation is shown in (G); relative size in (H).

(legend continued on next page)

(Bayarsaihan et al., 1998). Therefore, we performed homology modeling of mouse YB-1 and found there was a pocket-like structure in this protein (Figure 6A). Amino acids 42–53 (aas 42–53) in the N terminus of YB-1 were predicted to be important for this identified pocket-like structure formation; indeed, deletion of aas 42–53 in YB-1 disrupted the interaction between *Hnscr* and YB-1 (Figures S5C and S5D), which indicated that this pocket-like structure is crucial for YB-1 binding with *Hnscr*. To screen naturally occurring small-molecule compounds that target and stabilize YB-1, we performed molecular docking and virtual screening between YB-1 and the natural small molecular compounds library of Target Molecule (Target Mol), which contains more than 6,000 compounds. Considering the druggable criteria and binding affinity, we chose the 5 top-ranked small molecules as candidates (Tables S3 and S4). Among them, theaflavin 3-gallate (TF2A) was of particular interest, because the molecular docking results showed that it has the maximum affinity for YB-1 and could enter into the pocket-like structure of YB-1 (Figures 6B and 6C and Table S3). In support of this idea, western blotting results showed that only TF2A enhanced the expression levels of YB-1 in htNSCs derived from 3-month-old WT mice (Figures 6D and S6A–S6D). Treating htNSCs with TF2A increased the stability of YB-1 and protected it from ubiquitination-mediated degradation (Figures 6E and 6F), further suggesting that TF2A could act as a mimic of *Hnscr*.

TF2A Treatment *In Vitro* Reduces htNSC Senescence

The high homology between mouse and human YB-1 protein (Bayarsaihan et al., 1998) prompted us to investigate the effects of TF2A on YB-1 stability in htNSC-like cells derived from a line of human pluripotent stem cells (hPSCs). Using a previously published protocol (Li et al., 2014; Okada et al., 2004; Wataya et al., 2008; Waterhouse et al., 2012), we induced htNSC-like cells from hPSCs and confirmed that these cells were positive for Nestin and SOX2 and could differentiate into Tuj1-expressing neurons, O4-expressing oligodendrocytes, and GFAP-expressing astrocytes (Figure 6G). We induced senescence of these htNSC-like cells with 100 μM of buthionine sulfoximine (BSO) for 48 h and treated them with each of the selected 5 top-ranked small molecules, including TF2A, Didymin, Eriocitrin, Puerarin 6''-O-xylos, and 2,3,2,"3''-Tetrahydroochnaflavone. We found that TF2A treatment was the most remarkable in counteracting the effects of BSO in inducing cell senescence (Figure S6E). Using these htNSC-like cells, we further confirmed that TF2A treatment led to increased protein level of YB-1 (Figure 6H). These *in vitro* assays provided evidence indicating that TF2A bears a potential for suppressing NSC senescence.

TF2A Reduces htNSC Senescence and Aging-Related Physiological Decline

We investigated the potential role of TF2A in alleviating htNSCs senescence and whether it is sufficient to improve physiology at middle age. 12-month-old WT mice were administrated with TF2A at 8 mg/kg body weight/day or with vehicle for 6 months (Figure 7A). For 12-month-old WT mice, after treatment with TF2A for 6 months, the proliferation and differentiation of htNSCs derived from these mice increased significantly, as shown by the neurosphere assay, cell-proliferation-rate analysis, and cell-differentiation assay (Figures 7B–7G). Senescence of htNSCs derived from these mice were lower than those derived from vehicle-treated mice, as shown by SA-βGal staining (Figures 7H and 7I). Furthermore, $SOX2^{+}BMI1^{+}$ htNSCs were also significantly higher in the hypothalami of mice administrated with TF2A than in those of controls (Figure 7J). Through behavioral tests, we found that TF2A-treated middle-aged mice showed fewer behavioral declines than did vehicle-treated mice (Figures 7K–7N). The GTT and ITT results indicated that TF2A-treated aged mice showed improved glucose tolerance and insulin sensitivity in comparison with vehicle-treated mice (Figures S7A and S7B). The micro-CT analysis revealed that the bone mass of middle-aged mice increased after 6 months of TF2A administration in relation with vehicle-treated mice (Figures 7O and 7P). TF2A treatment also led to a slowing of reproductive decline during middle age as compared with vehicle-treated mice (Figures S7C–S7E).

Finally, we also assessed whether TF2A might have any obvious adverse effects. TF2A did not affect the body weight, blood cells, or blood biochemistry of mice (Figure S7F and Table S5). We also found that TF2A treatment did not result in appreciable cardiotoxicity, hepatotoxicity, spleen cell toxicity, pulmonary toxicity and nephrotoxicity (Figure S7G), nor cytotoxicity (Figure S7H). We also performed a tumorigenicity assay and found that TF2A treatment did not promote tumor development (Figure S7I). Thus, TF2A seems to be a relatively safe, naturally occurring compound.

DISCUSSION

Aging is characterized by a progressive loss of physiological integrity at the whole-body level. López-Otín et al. (2013) have summarized a list of mechanistic hallmarks that can contribute to the aging process, including genomic instability, telomere attrition, epigenetic alterations, loss of proteostasis, deregulated nutrient sensing, mitochondrial dysfunction, cellular senescence, stem-cell exhaustion, and altered intercellular communication (López-Otín et al., 2013). All these factors can interact with and are intertwined with each other, making the mechanisms of aging extremely complex. Among these topics, the potential role due to stem cell exhaustion has received some attention (Rossi et al., 2007; Villeda et al., 2011; Yilmaz et al., 2012). The hypothalamus, which is fundamental for regulating many basic functions of life, was recently suggested to play a role in systemic aging (Cai and Khor, 2019; Cavadas et al., 2016; Zhang et al., 2013; Zhang et al., 2017). Along these lines, htNSCs in the

(I and J) Representative images (n = 18 photographs from 3 experiments) of SA-βGal staining of dissociated htNSCs from mice 1 month after viral injection (I). Scale bar, 100 μm. The percentage of senescent cells is shown in (J).

(K) Cell output of dissociated htNSCs from mice 1 month after viral injection over 5 passages.

(L) The percentage of $SOX2^{+}BMI1^{+}$ cells in the hypothalamic third-ventricle wall and MBH parenchyma of mice 4 months after viral injection.

Data are shown as mean ± SEM. n = 6 in [E]–[L]. The cell experiments were repeated 3 times. *$p < 0.05$; **$p < 0.01$; ***$p < 0.001$ by two-tailed Student's t test or one-way ANOVA.

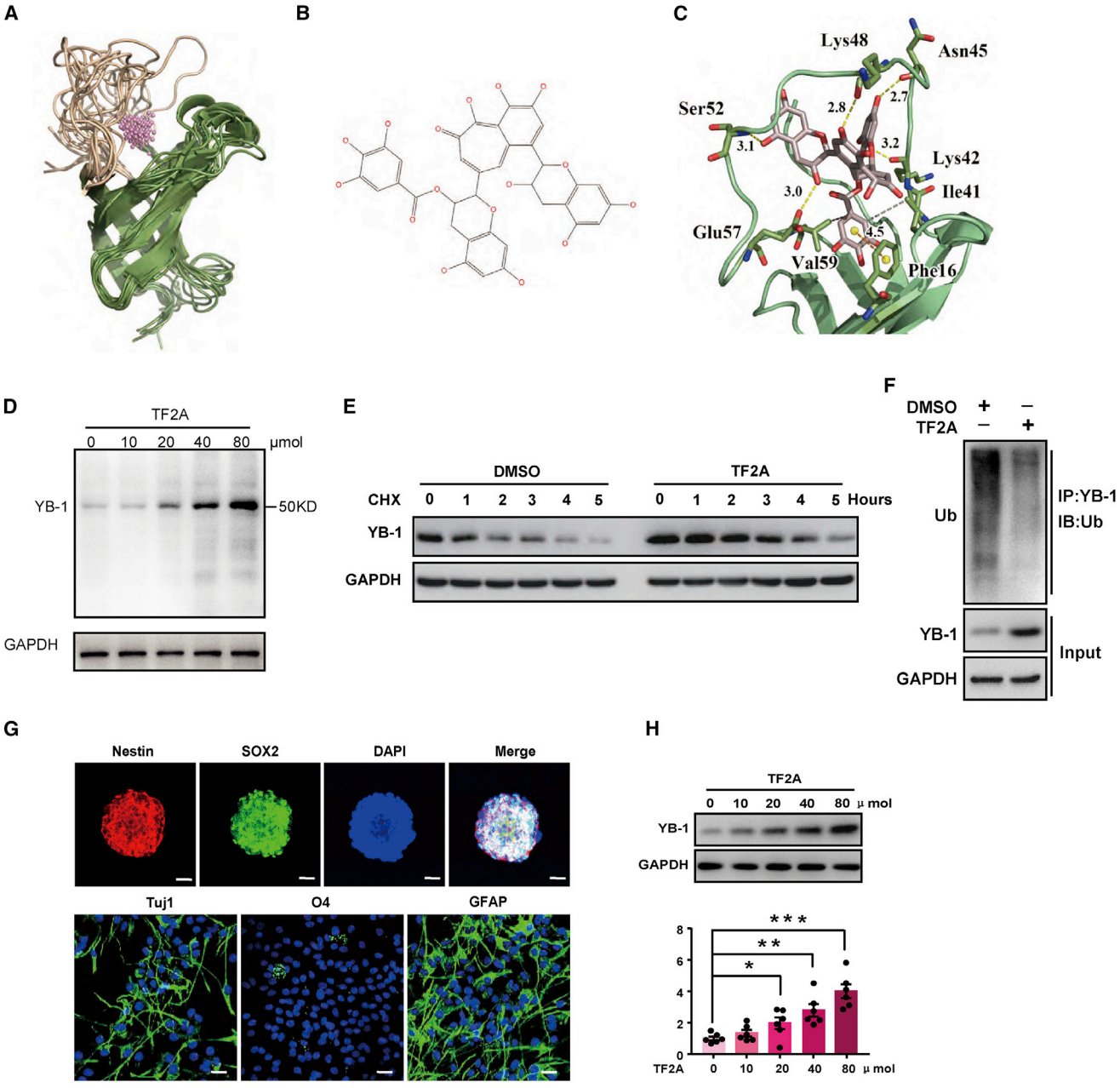

Figure 6. Theaflavin 3-gallate (TF2A) Acts as an *Hnscr* Mimic

(A) The optimized homology modeling structure of mouse YB-1. The green ribbon indicated a main barrel-like structure that is composed of 6 reverse-laminated beta-sheets. The upper part of the barrel-like structure (presented as the wheat-colored thread) indicated a dynamic loop area. Between them was the prediction of small molecule binding pockets (presented as pink balls) that consisted of 12 hydrophobic amino acids.

(B) The molecular structure of TF2A.

(C) The optimized binding modes with lowest binding energy generated by AutoDock Vina and key residues for interaction between TF2A and mouse YB-1.

(D) The expression of YB-1 in mouse htNSCs treated with TF2A in a series of doses, as indicated.

(E) The protein levels of YB-1 in TF2A pre-treated mouse htNSCs treated with cycloheximide (CHX).

(F) Western blot analysis of YB-1-associated ubiquitination in TF2A pre-treated mouse htNSCs treated with Mg132.

(G) Top: hPSCs derived neurospheres immunostained with Nestin and SOX2. Scale bar, 100 μm (n = 15 photographs from 3 experiments). Bottom: hPSC-derived NSCs were induced to differentiate after 7 days of differentiation. The cells were immunostained with neuronal marker Tuj1, oligodendrocyte marker O4, and astrocyte marker GFAP. Scale bar, 100 μm (n = 15 photographs from 3 experiments).

(H) The protein levels of YB-1 in hPSC-derived NSCs treated with TF2A in a series of dose as indicated. Top: representative images of western blot. Bottom: quantification analysis of YB-1 in relation to GAPDH.

Data are shown as mean ± SEM. The cell experiments were repeated 3 times. *$p < 0.05$; **$p < 0.01$; ***$p < 0.001$ by two-tailed Student's t test or one-way ANOVA.

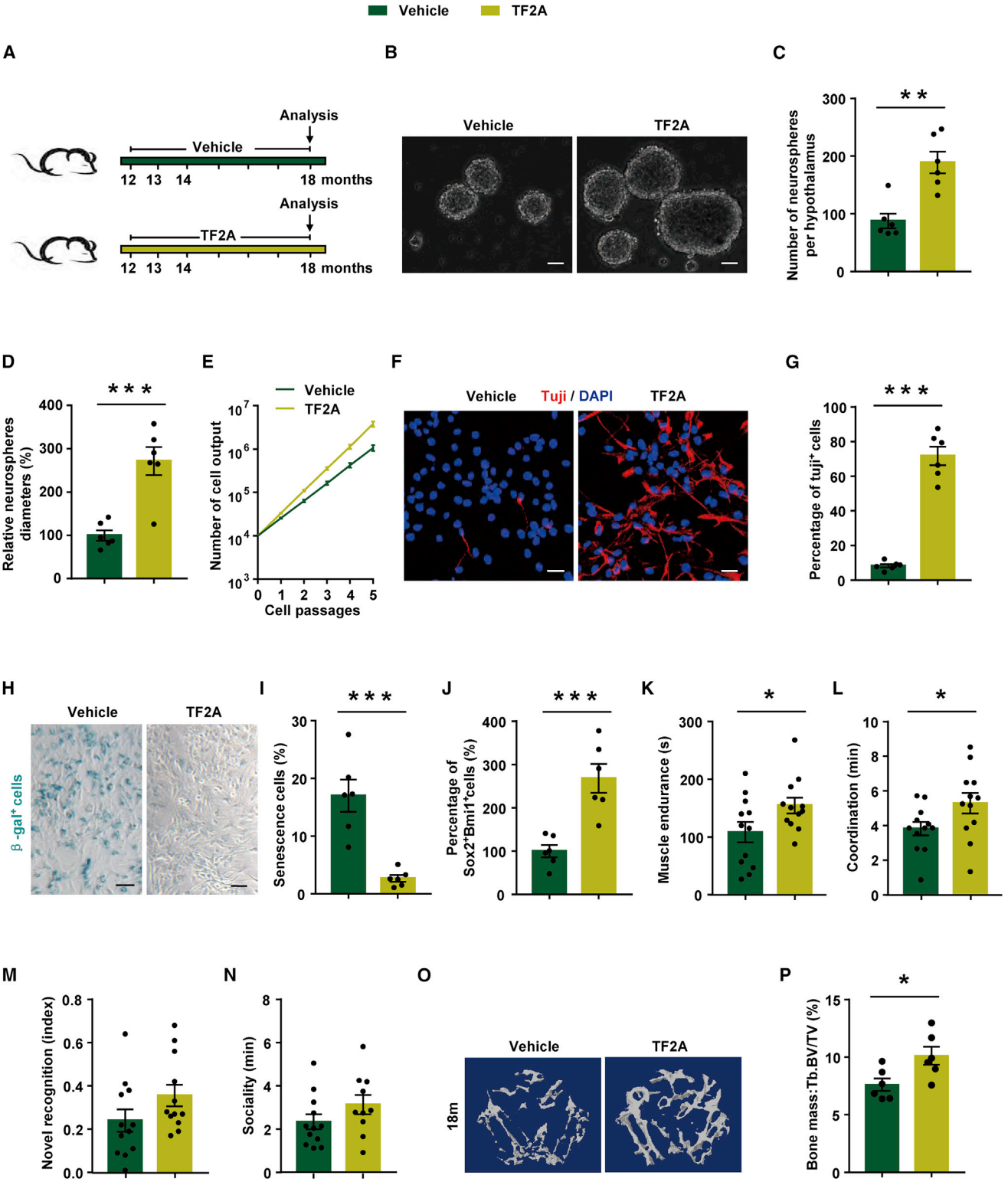

Figure 7. TF2A Treatment Leads to Reduction in htNSC Senescence and Aging

(A) Schematic of the time in which mice were orally administrated TF2A or vehicle.

(B–E) Representative images (n = 12 photographs from 2 experiments) of neurospheres generated from mice (B). Scale bar, 100 μm. Their quantitation is shown in (C); relative size in (D); and the cell output over 5 passages in (E).

(legend continued on next page)

hypothalamus have been demonstrated to be critical for the hypothalamic mechanism of regulating aging (Zhang et al., 2017). Notably, htNSCs abundantly release miRNAs-containing exosomes (Zhang et al., 2017), suggesting these cells have a unique endocrine function. Here, we found that htNSCs uniquely harbor certain lncRNAs that may have important roles in affecting the fate of these stem cells through regulation of cell senescence. Indeed, the existence of such lncRNAs are in line with the known role lncRNAs play in pluripotency maintenance and neurogenesis of embryonic stem cells (Ng et al., 2012), reprogramming of pluripotent stem cells (Loewer et al., 2010), and even self-renewal of cancer stem cells (Wang et al., 2015). Previously, our group found that *Hnscr* regulates the fate of bone marrow mesenchymal stem cells (BMSCs) during aging (Li et al., 2018). Through focusing on *Hnscr*, a lncRNA which is abundant in the htNSCs at early ages but dramatically decreases as mice age, we provide experimental models and evidence that illustrates the role of lncRNAs in the hypothalamic control of aging.

At the mechanistic level, we found that *Hnscr* regulated the senescence of htNSCs and the aging of mice via binding to YB-1 to protect it from ubiquitination and protein degradation. YB-1 is a multifunctional protein (Bernstein et al., 2015; Raffetseder et al., 2012) that is important for controlling protein translation (Bader et al., 2003; En-Nia et al., 2005), in addition to regulating DNA repair (Izumi et al., 2001). Kotake et al. (2013) demonstrated that YB-1 directly associates with the $p16^{INK4A}$ promoter to repress its expression. In this study, our results confirmed that YB-1 functions as a transcriptional repressor that inhibits the expression of $p16^{INK4A}$ in htNSCs. These findings suggest that YB-1 might be a potential molecular target to modulate htNSC senescence. Based on this molecular pathway, we performed molecular docking and virtual screening (Liang et al., 2018) to identify naturally occurring small-molecule compounds that could bind YB-1 and further alleviate htNSC senescence. One such hit in this screen is TF2A, which we also showed is a potential drug candidate to alleviate htNSC senescence and other hallmarks of aging. TF2A is an isomeric monomer of theaflavins, which are derived from black tea (Anandhan et al., 2012), but the relationship of this herb with health has only been empirically studied. Our results here showed that TF2A treatment helped improve the stability of YB-1, alleviated the senescence of htNSCs, and reduced the extent of aging-related physiological decline in mice. Although further evaluation of its efficacy and especially safety are still required in larger animals, TF2A could act as a lead compound in the design of new drugs that protect htNSC senescence and ameliorate some aspect of aging-related comorbidities. Taken together, this study revealed that the *Hnscr*–YB-1 signaling axis is critical for htNSC senescence and healthy aging of mice, and enhancement of this pathway could potentially offer a benefit during the aging process.

LIMITATIONS OF STUDY

One limitation of this work is that other lncRNAs besides *Hnscr* could be importantly involved in htNSC senescence and healthy aging. Further, we did not overexpress *Hnscr* in htNSCs of older mice to levels observed in younger mice to determine wheather such overexpression was sufficient to prevent senescence and improve physiological aging. Another limitation is related to the connection between *Hnscr* and YB-1. Although YB-1 is an important target of *Hnscr* in affecting the senescence of these cells, it might not be the only one, so future work is still needed to address other targets. Despite these limitations, we believe this study provides a convincing case that lncRNAs are important for understanding htNSC senescence and their physiological roles in aging-related pathology.

STAR★METHODS

Detailed methods are provided in the online version of this paper and include the following:

- KEY RESOURCES TABLE
- LEAD CONTACT AND MATERIALS AVAILABILITY
  - Materials Availability Statement
- EXPERIMENTAL MODELS AND SUBJECT DETAILS
  - Animals
  - Primary Cell Culture
- METHOD DETAILS
  - Hypothalamic Injection
  - Chemical Treatment
  - Behavioral Tests
  - Glucose and Insulin Tolerance Tests
  - Reproductive Fitness Test
  - Immunofluorescence Staining and Histology
  - htNSCs Proliferation, Differentiation and Senescence Assays
  - Human Pluripotent Stem Cells (hPSCs) and Derived NSCs
  - Plasmids and Recombinant Viruses
  - Luciferase Activity and ChIP Assays
  - RNA Pull-down Assay
  - RNA Immunoprecipitation
  - RNA Sequencing and Bioinformatics Analysis
  - Molecular Docking and Virtual Screening

(F and G) Representative images (n = 12 photographs from 2 experiments) of Tuj1 immunostaining of dissociated htNSCs from mice (F). Scale bar, 100 μm. The percentage of $Tuj1^+$ cells is shown in (G).

(H and I) Representative images (n = 12 photographs from 2 experiments) of SA-βGal staining of dissociated htNSCs from mice (H). Scale bar, 100 μm. The percentage of senescent cells is shown in (I).

(J) Relative percentage of $SOX2^+BMI1^+$ cells in the hypothalamic third-ventricle wall and MBH parenchyma of mice.

(K–N) The physiological changes including muscle endurance performance (K), coordination (L), novel object recognition (M), and sociality function (N) of mice at 6 months after TF2A administration.

(O and P) Representative micro-CT images (n = 12 photographs from 2 experiments) (O) and quantitative analysis (P) of femur of mice. Tb. BV/TV, trabecular bone volume per tissue volume.

Data are shown as mean ± SEM, (n = 6 in [B]–[J] and [O]–[P], n = 10–12 in [K]–[N]). *$p < 0.05$; **$p < 0.01$; ***$p < 0.001$ by two-tailed Student's t test or one-way ANOVA.

SUPPLEMENTAL INFORMATION

Supplemental Information can be found online at https://doi.org/10.1016/j.cmet.2020.01.002.

ACKNOWLEDGMENTS

The authors thank Prof. Qiurong Ding from Shanghai Institute of Nutrition and Health, Shanghai Institutes for Biological Sciences (SIBS), and the Chinese Academy of Sciences for providing hPSCs. They also thank Microanaly (Shanghai) Gene Technologies Co., Ltd for the kind help in RNA-seq data analysis. We thank Prof. Wei Li from State Key Laboratory of Stem Cell and Reproductive Biology, Institute of Zoology, and the Chinese Academy of Sciences for kind help in reproductive fitness test. This work was supported by grants from the National Natural Science Foundation of China (81930022, 91749105, 81520108008, 81700785, 81801393, 81873643), the Natural Science Foundation of Hunan Province of China (S2019JJQNJJ0681), the innovation-driven project of Central South University (20180033040008), the Science and Technology Development Plan of Hunan Province in 2017 (2017RS3014), and the Talent Plan of Xiangya Hospital at Central South University (grants 52 and 35).

AUTHOR CONTRIBUTIONS

Y.Z.X. designed the experiments, generated data, and drafted the manuscript; Y.Z.X., M.Y., and Y.X. carried out majority of the experiments; Q.G., Y.H., and C.J.L. contributed to sample collection; D.C. co-advised the study, guided experiments, and co-wrote the manuscript; X.H.L. supervised the experiments, analyzed results, co-wrote the manuscript, and is the guarantor of this work with full access to all the data in this study, taking the responsibility for data accuracy.

DECLARATION OF INTERESTS

The authors declare no competing interests.

Received: March 11, 2019
Revised: November 15, 2019
Accepted: January 6, 2020
Published: January 30, 2020

REFERENCES

Akerman, I., Tu, Z., Beucher, A., Rolando, D.M.Y., Sauty-Colace, C., Benazra, M., Nakic, N., Yang, J., Wang, H., Pasquali, L., et al. (2017). Human Pancreatic β Cell lncRNAs Control Cell-Specific Regulatory Networks. Cell Metab. *25*, 400–411.

Anandhan, A., Tamilselvam, K., Radhiga, T., Rao, S., Essa, M.M., and Manivasagam, T. (2012). Theaflavin, a black tea polyphenol, protects nigral dopaminergic neurons against chronic MPTP/probenecid induced Parkinson's disease. Brain Res. *1433*, 104–113.

Arab, K., Park, Y.J., Lindroth, A.M., Schäfer, A., Oakes, C., Weichenhan, D., Lukanova, A., Lundin, E., Risch, A., Meister, M., et al. (2014). Long noncoding RNA TARID directs demethylation and activation of the tumor suppressor TCF21 via GADD45A. Mol. Cell *55*, 604–614.

Bader, A.G., Felts, K.A., Jiang, N., Chang, H.W., and Vogt, P.K. (2003). Y box-binding protein 1 induces resistance to oncogenic transformation by the phosphatidylinositol 3-kinase pathway. Proc. Natl. Acad. Sci. USA *100*, 12384–12389.

Bayarsaihan, D., Soto, R.J., and Lukens, L.N. (1998). Cloning and characterization of a novel sequence-specific single-stranded-DNA-binding protein. Biochem. J. *331*, 447–452.

Bernstein, H.-G., Lindquist, J.A., Keilhoff, G., Dobrowolny, H., Brandt, S., Steiner, J., Bogerts, B., and Mertens, P.R. (2015). Differential distribution of Y-box-binding protein 1 and cold shock domain protein A in developing and adult human brain. Brain Struct. Funct. *220*, 2235–2245.

Cai, D., and Khor, S. (2019). "Hypothalamic Microinflammation" Paradigm in Aging and Metabolic Diseases. Cell Metab. *30*, 19–35.

Cavadas, C., Aveleira, C.A., Souza, G.F., and Velloso, L.A. (2016). The pathophysiology of defective proteostasis in the hypothalamus - from obesity to ageing. Nat. Rev. Endocrinol. *12*, 723–733.

Deng, Y., Xiao, Y., Yuan, F., Liu, Y., Jiang, X., Deng, J., Fejes-Toth, G., Naray-Fejes-Toth, A., Chen, S., Chen, Y., et al. (2018). SGK1/FOXO3 Signaling in Hypothalamic POMC Neurons Mediates Glucocorticoid-Increased Adiposity. Diabetes *67*, 569–580.

Ding, Q., Lee, Y.K., Schaefer, E.A., Peters, D.T., Veres, A., Kim, K., Kuperwasser, N., Motola, D.L., Meissner, T.B., Hendriks, W.T., et al. (2013). A TALEN genome-editing system for generating human stem cell-based disease models. Cell Stem Cell *12*, 238–251.

Dong, W., Wang, H., Shahzad, K., Bock, F., Al-Dabet, M.M., Ranjan, S., Wolter, J., Kohli, S., Hoffmann, J., Dhople, V.M., et al. (2015). Activated Protein C Ameliorates Renal Ischemia-Reperfusion Injury by Restricting Y-Box Binding Protein-1 Ubiquitination. J. Am. Soc. Nephrol. *26*, 2789–2799.

En-Nia, A., Yilmaz, E., Klinge, U., Lovett, D.H., Stefanidis, I., and Mertens, P.R. (2005). Transcription factor YB-1 mediates DNA polymerase alpha gene expression. J. Biol. Chem. *280*, 7702–7711.

Esposito, K., Chiodini, P., Colao, A., Lenzi, A., and Giugliano, D. (2012). Metabolic syndrome and risk of cancer: a systematic review and meta-analysis. Diabetes Care *35*, 2402–2411.

Fry, C.S., Lee, J.D., Mula, J., Kirby, T.J., Jackson, J.R., Liu, F., Yang, L., Mendias, C.L., Dupont-Versteegden, E.E., McCarthy, J.J., and Peterson, C.A. (2015). Inducible depletion of satellite cells in adult, sedentary mice impairs muscle regenerative capacity without affecting sarcopenia. Nat. Med. *21*, 76–80.

Guo, W., Liu, S., Cheng, Y., Lu, L., Shi, J., Xu, G., Li, N., Cheng, K., Wu, M., Cheng, S., and Liu, S. (2016). ICAM-1-Related Noncoding RNA in Cancer Stem Cells Maintains ICAM-1 Expression in Hepatocellular Carcinoma. Clin. Cancer Res. *22*, 2041–2050.

Guttman, M., and Rinn, J.L. (2012). Modular regulatory principles of large non-coding RNAs. Nature *482*, 339–346.

Holzenberger, M., Dupont, J., Ducos, B., Leneuve, P., Géloën, A., Even, P.C., Cervera, P., and Le Bouc, Y. (2003). IGF-1 receptor regulates lifespan and resistance to oxidative stress in mice. Nature *421*, 182–187.

Hu, X., Feng, Y., Zhang, D., Zhao, S.D., Hu, Z., Greshock, J., Zhang, Y., Yang, L., Zhong, X., Wang, L.P., et al. (2014). A functional genomic approach identifies FAL1 as an oncogenic long noncoding RNA that associates with BMI1 and represses p21 expression in cancer. Cancer Cell *26*, 344–357.

Izumi, H., Imamura, T., Nagatani, G., Ise, T., Murakami, T., Uramoto, H., Torigoe, T., Ishiguchi, H., Yoshida, Y., Nomoto, M., et al. (2001). Y box-binding protein-1 binds preferentially to single-stranded nucleic acids and exhibits 3′–>5′ exonuclease activity. Nucleic Acids Res. *29*, 1200–1207.

Jürchott, K., Bergmann, S., Stein, U., Walther, W., Janz, M., Manni, I., Piaggio, G., Fietze, E., Dietel, M., and Royer, H.-D. (2003). YB-1 as a cell cycle-regulated transcription factor facilitating cyclin A and cyclin B1 gene expression. J. Biol. Chem. *278*, 27988–27996.

Kloks, C.P.A.M., Spronk, C.A.E.M., Lasonder, E., Hoffmann, A., Vuister, G.W., Grzesiek, S., and Hilbers, C.W. (2002). The solution structure and DNA-binding properties of the cold-shock domain of the human Y-box protein YB-1. J. Mol. Biol. *316*, 317–326.

Knoll, M., Lodish, H.F., and Sun, L. (2015). Long non-coding RNAs as regulators of the endocrine system. Nat. Rev. Endocrinol. *11*, 151–160.

Kotake, Y., Ozawa, Y., Harada, M., Kitagawa, K., Niida, H., Morita, Y., Tanaka, K., Suda, T., and Kitagawa, M. (2013). YB1 binds to and represses the p16 tumor suppressor gene. Genes Cells *18*, 999–1006.

Li, J., Tang, Y., and Cai, D. (2012). IKKβ/NF-κB disrupts adult hypothalamic neural stem cells to mediate a neurodegenerative mechanism of dietary obesity and pre-diabetes. Nat. Cell Biol. *14*, 999–1012.

Li, J., Tang, Y., Purkayastha, S., Yan, J., and Cai, D. (2014). Control of obesity and glucose intolerance via building neural stem cells in the hypothalamus. Mol. Metab. *3*, 313–324.

Li, C.J., Cheng, P., Liang, M.K., Chen, Y.S., Lu, Q., Wang, J.Y., Xia, Z.Y., Zhou, H.D., Cao, X., Xie, H., et al. (2015). MicroRNA-188 regulates age-related switch between osteoblast and adipocyte differentiation. J. Clin. Invest. *125*, 1509–1522.

Li, C.-J., Xiao, Y., Yang, M., Su, T., Sun, X., Guo, Q., Huang, Y., and Luo, X.-H. (2018). Long noncoding RNA Bmncr regulates mesenchymal stem cell fate during skeletal aging. J. Clin. Invest. *128*, 5251–5266.

Liang, C., Peng, S., Li, J., Lu, J., Guan, D., Jiang, F., Lu, C., Li, F., He, X., Zhu, H., et al. (2018). Inhibition of osteoblastic Smurf1 promotes bone formation in mouse models of distinctive age-related osteoporosis. Nat. Commun. *9*, 3428.

Liu, B., Sun, L., Liu, Q., Gong, C., Yao, Y., Lv, X., Lin, L., Yao, H., Su, F., Li, D., et al. (2015). A cytoplasmic NF-κB interacting long noncoding RNA blocks IκB phosphorylation and suppresses breast cancer metastasis. Cancer Cell *27*, 370–381.

Liu, C., Song, Z., Wang, L., Yu, H., Liu, W., Shang, Y., Xu, Z., Zhao, H., Gao, F., Wen, J., et al. (2017). Sirt1 regulates acrosome biogenesis by modulating autophagic flux during spermiogenesis in mice. Development *144*, 441–451.

Loewer, S., Cabili, M.N., Guttman, M., Loh, Y.-H., Thomas, K., Park, I.H., Garber, M., Curran, M., Onder, T., Agarwal, S., et al. (2010). Large intergenic non-coding RNA-RoR modulates reprogramming of human induced pluripotent stem cells. Nat. Genet. *42*, 1113–1117.

López-Otín, C., Blasco, M.A., Partridge, L., Serrano, M., and Kroemer, G. (2013). The hallmarks of aging. Cell *153*, 1194–1217.

Lu, Z.H., Books, J.T., and Ley, T.J. (2005). YB-1 is important for late-stage embryonic development, optimal cellular stress responses, and the prevention of premature senescence. Mol. Cell. Biol. *25*, 4625–4637.

Lu, Y., Zhao, X., Liu, Q., Li, C., Graves-Deal, R., Cao, Z., Singh, B., Franklin, J.L., Wang, J., Hu, H., et al. (2017). lncRNA MIR100HG-derived miR-100 and miR-125b mediate cetuximab resistance via Wnt/β-catenin signaling. Nat. Med. *23*, 1331–1341.

Ng, S.-Y., Johnson, R., and Stanton, L.W. (2012). Human long non-coding RNAs promote pluripotency and neuronal differentiation by association with chromatin modifiers and transcription factors. EMBO J. *31*, 522–533.

Okada, Y., Shimazaki, T., Sobue, G., and Okano, H. (2004). Retinoic-acid-concentration-dependent acquisition of neural cell identity during in vitro differentiation of mouse embryonic stem cells. Dev. Biol. *275*, 124–142.

Premsrirut, P.K., Dow, L.E., Kim, S.Y., Camiolo, M., Malone, C.D., Miething, C., Scuoppo, C., Zuber, J., Dickins, R.A., Kogan, S.C., et al. (2011). A rapid and scalable system for studying gene function in mice using conditional RNA interference. Cell *145*, 145–158.

Raffetseder, U., Liehn, E.A., Weber, C., and Mertens, P.R. (2012). Role of cold shock Y-box protein-1 in inflammation, atherosclerosis and organ transplant rejection. Eur. J. Cell Biol. *91*, 567–575.

Ransohoff, J.D., Wei, Y., and Khavari, P.A. (2018). The functions and unique features of long intergenic non-coding RNA. Nat. Rev. Mol. Cell Biol. *19*, 143–157.

Rossi, D.J., Bryder, D., Seita, J., Nussenzweig, A., Hoeijmakers, J., and Weissman, I.L. (2007). Deficiencies in DNA damage repair limit the function of haematopoietic stem cells with age. Nature *447*, 725–729.

Su, T., Xiao, Y., Xiao, Y., Guo, Q., Li, C., Huang, Y., Deng, Q., Wen, J., Zhou, F., and Luo, X.-H. (2019). Bone Marrow Mesenchymal Stem Cells-Derived Exosomal MiR-29b-3p Regulates Aging-Associated Insulin Resistance. ACS Nano *13*, 2450–2462.

Tang, Y., and Cai, D. (2013). Hypothalamic inflammation and GnRH in aging development. Cell Cycle *12*, 2711–2712.

van Roeyen, C.R.C., Scurt, F.G., Brandt, S., Kuhl, V.A., Martinkus, S., Djudjaj, S., Raffetseder, U., Royer, H.-D., Stefanidis, I., Dunn, S.E., et al. (2013). Cold shock Y-box protein-1 proteolysis autoregulates its transcriptional activities. Cell Commun. Signal. *11*, 63.

Villeda, S.A., Luo, J., Mosher, K.I., Zou, B., Britschgi, M., Bieri, G., Stan, T.M., Fainberg, N., Ding, Z., Eggel, A., et al. (2011). The ageing systemic milieu negatively regulates neurogenesis and cognitive function. Nature *477*, 90–94.

Wang, Y., He, L., Du, Y., Zhu, P., Huang, G., Luo, J., Yan, X., Ye, B., Li, C., Xia, P., et al. (2015). The long noncoding RNA lncTCF7 promotes self-renewal of human liver cancer stem cells through activation of Wnt signaling. Cell Stem Cell *16*, 413–425.

Wataya, T., Ando, S., Muguruma, K., Ikeda, H., Watanabe, K., Eiraku, M., Kawada, M., Takahashi, J., Hashimoto, N., and Sasai, Y. (2008). Minimization of exogenous signals in ES cell culture induces rostral hypothalamic differentiation. Proc. Natl. Acad. Sci. USA *105*, 11796–11801.

Waterhouse, E.G., An, J.J., Orefice, L.L., Baydyuk, M., Liao, G.Y., Zheng, K., Lu, B., and Xu, B. (2012). BDNF promotes differentiation and maturation of adult-born neurons through GABAergic transmission. J. Neurosci. *32*, 14318–14330.

Wong, C.M., Tsang, F.H., and Ng, I.O. (2018). Non-coding RNAs in hepatocellular carcinoma: molecular functions and pathological implications. Nat. Rev. Gastroenterol. Hepatol. *15*, 137–151.

Xiao, Y., Deng, Y., Yuan, F., Xia, T., Liu, H., Li, Z., Liu, Z., Ying, H., Liu, Y., Zhai, Q., et al. (2017). ATF4/ATG5 Signaling in Hypothalamic Proopiomelanocortin Neurons Regulates Fat Mass via Affecting Energy Expenditure. Diabetes *66*, 1146–1158.

Yang, M., Li, C.-J., Sun, X., Guo, Q., Xiao, Y., Su, T., Tu, M.-L., Peng, H., Lu, Q., Liu, Q., et al. (2017). MiR-497:195 cluster regulates angiogenesis during coupling with osteogenesis by maintaining endothelial Notch and HIF-1α activity. Nat. Commun. *8*, 16003.

Yang, M., Guo, Q., Peng, H., Xiao, Y.-Z., Xiao, Y., Huang, Y., Li, C.-J., Su, T., Zhang, Y.-L., Lei, M.-X., et al. (2019). Krüppel-like factor 3 inhibition by mutated lncRNA *Reg1cp* results in human high bone mass syndrome. J. Exp. Med. *216*, 1944–1964.

Yilmaz, Ö.H., Katajisto, P., Lamming, D.W., Gültekin, Y., Bauer-Rowe, K.E., Sengupta, S., Birsoy, K., Dursun, A., Yilmaz, V.O., Selig, M., et al. (2012). mTORC1 in the Paneth cell niche couples intestinal stem-cell function to calorie intake. Nature *486*, 490–495.

Zhang, G., Li, J., Purkayastha, S., Tang, Y., Zhang, H., Yin, Y., Li, B., Liu, G., and Cai, D. (2013). Hypothalamic programming of systemic ageing involving IKK-β, NF-κB and GnRH. Nature *497*, 211–216.

Zhang, Y., Kim, M.S., Jia, B., Yan, J., Zuniga-Hertz, J.P., Han, C., and Cai, D. (2017). Hypothalamic stem cells control ageing speed partly through exosomal miRNAs. Nature *548*, 52–57.

Zhao, X.Y., Li, S., Wang, G.X., Yu, Q., and Lin, J.D. (2014). A long noncoding RNA transcriptional regulatory circuit drives thermogenic adipocyte differentiation. Mol. Cell *55*, 372–382.

STAR★METHODS

KEY RESOURCES TABLE

REAGENT or RESOURCE	SOURCE	IDENTIFIER
Antibodies		
Anti-SOX2	Millipore	Cat# AB5603; RRID: AB_2286686
Anti-NeuN	Millipore	Cat# MAB377; RRID: AB_2298772
Mouse anti-GFAP	Millipore	Cat# 04-1062; RRID: AB_1977213
Mouse anti-O4	Millipore	Cat# MAB345; RRID: AB_11213138
Anti-BMI1	Abcam	Cat# ab14389; RRID: AB_2065390
Anti-NPY	Abcam	Cat# ab10980; RRID: AB_297635
Anti-POMC	phoenix	Cat# H-029-30; RRID: AB_2307442
Anti-YB-1	Santa Cruz Biotechnology	Cat# sc-398146
Mouse anti-Tuj1	Cell Signaling Technology	Cat# 4466; RRID: AB_1904176
Rabbit anti-YB-1	Cell Signaling Technology	Cat# 9744; RRID: AB_11178953
Mouse anti-Ubiquitin	Cell Signaling Technology	Cat# 3936; RRID: AB_331292)
Rabbit anti-p16^{INK4A}	Cell Signaling Technology	Cat# 92803; RRID: AB_2750891
Rabbit anti-GAPDH	Cell Signaling Technology	Cat# 5174; RRID: AB_10622025
Bacterial and Virus Strains		
Adeno-associated viruses	Obio Technology (Shanghai) Corp., Ltd.	N/A
Lentiviral vector: pHBLV-CMV-IRES-Puro vector	Hanbio Biotechnology, Shanghai, China	N/A
Lentiviral vector: pHBLV-U6-Puro vector	Hanbio Biotechnology, Shanghai, China	N/A
Chemicals, Peptides, and Recombinant Proteins		
Theaflavin 3-gallate (TF2A)	Wako	202-15191
Didymin	TargetMol	T3787
Eriocitrin	TargetMol	T6S0221
Puerarin 6''-O-xyloside	Biorbyt	orb259460
2,3,2,"3''-Tetrahydroochnaflavone	Chem Faces	CFN97157
TrypLE Express enzyme	Invitrogen,Life Technologies	12563029
Neurobasal-A	Invitrogen,Life Technologies	10888022
GlutaMAX supplement	Invitrogen,Life Technologies	35050061
B27 without vitamin A	Invitrogen,Life Technologies	12587010
Bfgf	Invitrogen,Life Technologies	13256029
Fetal bovine serum	GIBCO,Life Technologies	10099141
Geltrex matrix	Invitrogen	A1413202
Accutase	Invitrogen	A1110501
N2 Supplement	Life Technologies	17502001
EGF	Sigma-Aldrich	E4127
Poly-D-Lysine & Laminin	Sigma	127
Retinoic Acid	Sigma	R3375
mTeSR1 medium	STEMCELL Technologies	05850
Critical Commercial Assays		
Senescence β-galactosidase staining Kit	Cell Signaling Technology	9860
Magna RIP RNA-Binding Protein Immunoprecipitation Kit	Millipore	17-700
Deposited Data		
RNASeq data	This paper	PRJNA505113

(*Continued on next page*)

Continued

REAGENT or RESOURCE	SOURCE	IDENTIFIER
Experimental Models: Cell Lines		
HEK293T	ATCC	CRL-3216
hPSCs	ATCC	ACS-1011
Experimental Models: Organisms/Strains		
C57/BL6J mice	Shanghai SLAC Laboratory Animals Co. Ltd	N/A
Gm31629 knockout mice	This paper	N/A
Oligonucleotides		
See Table S6 for qPCR primers	This paper	N/A
Recombinant DNA		
Plasmid: pCMV3-HA-mYbx1 del pocket	This paper	N/A
Plasmid: pCMV3-HA-mYbx1 del C	This paper	N/A
Plasmid: pCMV3-HA-mYbx1 del N	This paper	N/A
Plasmid: pCMV3-HA-mYbx1 del CSD	This paper	N/A
Plasmid: YBX1- C-HA tag	Sino biological inc	MG51594-CY
Software and Algorithms		
CASA	CEROS V.12, Hamilton Thorne Research	https://www.hamiltonthorne.com
ImageJ	NIH	https://imagej.nih.gov/ij/
Software Ideas Modeler	Dušan Rodina	https://www.softwareideas.net/
NRecon v1.6	Bioz, Inc., Palo Alto	https://www.microphotonics.com/products/micro-ct/nrecon-reconstruction-software/
CT Analyzer v1.9	Bruker microCT	https://www.bruker.com
μCT Volume v2.0	Bruker microCT	https://www.bruker.com
GraphPad Prism 7.0	GraphPad Software	http://www.graphpad.com
SPSS 20.0	IBM Company	https://www.ibm.com/products/spss-statistics

LEAD CONTACT AND MATERIALS AVAILABILITY

Materials Availability Statement

All the data and materials that support the findings of this study are available within the article and supplementary files or available from the authors upon request.

Further information and requests for resources and reagents should be directed to and will be fulfilled by the Lead Contact, Xiang-Hang Luo (xianghangluo@sina.com).

EXPERIMENTAL MODELS AND SUBJECT DETAILS

Animals

C57BL/6J mice were obtained from Shanghai SLAC Laboratory Animals Co. Ltd (Shanghai, China). To generate *Hnscr* null mice, the genome region of mouse *Gm31629* gene was knocked out by the TetraOne™ technique from Cyagen Biosciences Inc (China). For genotyping of *Hnscr*, genomic DNA from the toes or tail of newborn mice was extracted, and PCR was carried out by the following primers: F:5′-GCTAAGCTCGAGGGACCTAATA-3′; R: 5′-AGGGATGTTCCTCACTGGCTGG-3′. All mice were kept on the C57BL/6J background and maintained in standard, specific pathogen-free facility of the Laboratory Animal Research Center of Central South University, with the temperature at 22-24°C and a 12 h dark/light cycle and 4–5 mice per cage. All mice health status was monitored on daily basis and abnormalities reported to facility veterinarian. In this study, male mice at 3 months or 18 months old were used unless specified otherwise. All mice were kept on a standard normal chow diet purchased from Shanghai Laboratory Animals Co. Ltd (Shanghai, China). All animal care protocols and experiments were reviewed and approved by the Animal Care and Use Committees of the Laboratory Animal Research Center at Xiangya Medical School of Central South University, and this study was compliant with all relevant ethical regulations regarding animal research.

Primary Cell Culture

The primary culture of hypothalamic neural stem cells was performed as described previously (Esposito et al., 2012; Li et al., 2014; Zhang et al., 2017). In brief, the hypothalamic tissues of mice were isolated and cut into small pieces (approximately 1 mm^3), and followed by digested with TrypLE Express enzyme (Invitrogen, Life Technologies) for 30 min at 37°C. After filtration and centrifugation, the cells were suspended in growth medium composed of neurobasal-A (Invitrogen, Life Technologies), 0.24% GlutaMAX supplement (Invitrogen, Life Technologies), 4% B27 without vitamin A (Invitrogen, Life Technologies), 20 ng ml-1 EGF (Sigma-Aldrich), 20 ng ml-1 bFGF (Invitrogen, Life Technologies) and seeded in ultralow-adhesion 6-well plates (Corning) at the density of 10^6 cells per well. 7-10 days later, the neurospheres were captured and collected by centrifugation, then, dissociated into single cells and passaged to form further generation of neurospheres until experimental use. For neurosphere counting, the neurospheres were counted under a microscope. For quantification of the neurosphere size, the diameters of captured neurospheres were measured by the ImageJ software program.

METHOD DETAILS

Hypothalamic Injection

Purified AAVs were bilaterally intra-MBH injected as previously (Deng et al., 2018; Zhang et al., 2017). Briefly, Adeno-associated viruses were suspended in 0.5 μL artificial cerebrospinal fluid (aCSF), then, bilaterally intra-MBH injected to mice by an ultra-precise stereotactic equipment (Stoelting Instruments). The coordinate is 5.8 mm below the surface of the skull; 1.7mm posterior to bregma; and 0.23 mm lateral to the midline of the brain, and the AAVs were injected via a gauge guide cannula and a gauge internal injector, which connected to a 5 μL Hamilton syringe and infusion pump (WPI Instruments).

Chemical Treatment

Theaflavin 3-gallate (TF2A) was purchased from Wako (202-15191), Didymin (T3787) and Eriocitrin (T6S0221) were purchased from TargetMol, Puerarin 6''-O-xyloside and 2,3,2,"3''-Tetrahydroochnaflavone were purchased from Biorbyt (orb259460) or *Chem Faces* (CFN97157) respectively. For animal studies, TF2A was administrated by oral gavage at the dose of 8 mg/kg/day daily for six months; for cell experiments, TF2A, Didymin, Eriocitrin, Puerarin 6''-O-xyloside and 2,3,2,"3''-Tetrahydroochnaflavone were dissolved in DMSO or PBS and treated as the concentration indicated for 72 h.

Behavioral Tests

All the behavior tests were performed in a behavioral testing room as reported previously (Fry et al., 2015; Tang and Cai, 2013; Zhang et al., 2013; Zhang et al., 2017). A video tracking system (Stoelting) connected with a digital camera was used to videotape the animal activities in training and experimental sessions of behavioral tests.

Glucose and Insulin Tolerance Tests

The glucose tolerance tests (GTTs) and insulin tolerance tests (ITTs) were performed as reported previously (Su et al., 2019). For GTTs, mice were intraperitoneally treated with glucose at dosage of 1g/kg after overnight fast. For ITTs, mice were intraperitoneally treated with insulin at dosage of 0.75U/kg after 6 h fast. Blood was collected by venous bleeding from the tail vein at 0, 15, 30, 60, and 120 min after glucose or insulin injection, and glucose concentrations were measured by glucometer.

Reproductive Fitness Test

The Reproductive fitness test was performed as reported previously (Holzenberger et al., 2003; Liu et al., 2017). To isolate the sperm, epididymis and the first few millimeters of the vas deferens were isolated and transferred to 1ml human tubal fluid (HTF). Then the epididymis was dissected and incubated for 30 min at 37 to allow the sperm to be released. The suspension was pipetted and filtered through 80 μm nylon mesh to remove tissue fragments. 10 ul of the exudate was placed into a glass cell chamber (Leja Products BV, Nieuw-Vennep, the Netherlands). The sperms were viewed using an Olympus microscope and analyzed using CASA (CEROS V.12, Hamilton Thorne Research) implemented using the Minitube Sperm Vison Digital Semen Evaluation System (12500/1300, Minitube Group, Tiefenbach, Germany). For female fertility test, we mated female mice with fertile males for three weeks and recorded the resulting pregnancies and offspring.

Immunofluorescence Staining and Histology

Immunofluorescence staining was performed as reported previously (Deng et al., 2018; Yang et al., 2019). Briefly, the mice were anesthesia and perfused with 4% paraformaldehyde transcardially. Then, the brains were isolated, post-fixed and infiltrated with 20% sucrose, 30% sucrose orderly. Brain slices with the thickness of 25 μm were cut by a vibration slicer (Leica Instruments), and blocked with the serum of secondary antibody's species, then, treated with primary antibodies as following, anti-SOX2 (Millipore, AB5603) and anti-BMI1 (Abcam, ab14389). Anti-NeuN (Millipore, MAB 377), anti-POMC (phoenix, H-029-30), anti-NPY (Abcam, ab10980). Subsequently, the brain slides were incubated with AlexaFluor 488 or 555 secondary antibodies. For cell immunofluorescence, the primary antibodies are mouse anti-Tuj1 (Cell Signaling Technology, 4466), mouse anti-O4 (Millipore, MAB345) and mouse anti-GFAP (Millipore, 04-1062). All the fluorescence pictures were captured by a confocal microscope. Cells of interest were counted and calculated. For tissue histology, quadriceps, dorsal skin, heart, liver, spleen, lung and kidney were dissected and fixed in 4%

paraformaldehyde at 4°C overnight, then, embedded into paraffin. Paraffin sections with the thickness of 6-μm were prepared and stained with hematoxylin and eosin for tissue histology.

htNSCs Proliferation, Differentiation and Senescence Assays

For the htNSCs proliferation output assay, the neurospheres were dissociated and seeded in ultralow adhesion 6-well culture plates at a density of 10^4 cells per 1 mL of growth medium, cells were passaged every 5 days at the same density for five generations. The viability of cells in each generation was evaluated by trypan blue staining. The accumulated total cell number for each generation was calculated on the assumption that the total cells from the previous generation were passaged. For htNSCs differentiation assay, dissociated single cells were seeded on coverslips that were coated by Poly-D-Lysine & Laminin (Sigma) and placed in 12-well plates. The cells were cultured in differentiation medium (Neurobasal-A, 2% B27 and 1% fetal bovine serum (GIBCO, Life Technologies) and 1 μM retinoic acid). The differentiation medium was changed every two days, and neural differentiation was induced in about one week. For cell senescence assay, the dissociated single cells were seeded in 6-well plates that were coated with Poly-D-Lysine & Laminin. After 24 h's culture, the senescent cells were stained by a senescence β-galactosidase staining Kit (Cell Signaling Technology, 9860), according to the manufacturer's instructions.

Human Pluripotent Stem Cells (hPSCs) and Derived NSCs

hPSCs were cultured and induced to differentiate into NSCs as described previously (Ding et al., 2013; Li et al., 2014; Okada et al., 2004; Wataya et al., 2008; Waterhouse et al., 2012). In brief, the hPSCs were cultured in feeder-free medium: mTeSR1 (STEMCELL Technologies, 05850) supplemented with penicillin and streptomycin. All the plates used were pre-coated with Geltrex matrix (Invitrogen, A1413202), the cells were dissociated with accutase (Invitrogen, A1110501) and regularly passaged. For embryoid body (EB) formation, the dissociated cells were cultured in DMEM/F12 containing 2% B27 and 1% N2 (Life Technologies). Following 4 days of EB formation, the cultured cells were stimulated with 10 mM Retinoic Acid (Sigma) for 10 days with the culture medium changed every day. At Day 15, EBs were dissociated into single cells and cultured in NSC medium (neurobasal-A containing 0.24% GlutaMAX supplement, 2% B27 without vitamin A, 10 ng ml-1 EGF and 10 ng ml-1 bFGF). Neurospheres were formed after 3-4 passages of culture as confirmed by immunostaining of NSC markers and the ability to differentiate into Tuj1-expressing neurons, O4-expressing oligodendrocytes and GFAP-expressing astrocytes. For neuropeptide treatment: the hPSCs derived NSCs were cultured in NSC medium supplemented with NPY (30 ng/mL) and BDNF (30 ng/mL) for 8 days, with medium changed every 2 days.

Plasmids and Recombinant Viruses

The AAV of Sox2 promoter driven *Hnscr* knockdown was generated by replacing the *Hnscr* transcript sequence with miR30-based shRNAs target for *Hnscr* in the above Sox2 promoter driven *Hnscr* overexpression plasmid (Premsrirut et al., 2011). The AAV vector of Sox2 promoter driven YB-1 overexpression was generated by replacing the *SYN* promoter with *Sox2* promoter and inserting the Open Reading Frame (ORF) of YB-1 to the MCS sites of pAAV-SYN-MCS-EGFP-3FLAG plasmid. AAVs were generated under the help of Obio Technology (Shanghai) Corp.,Ltd. Lentiviral vector driven *Hnscr* overexpression was generated by inserting the transcript sequence of *Hnscr* to pHBLV-CMV-IRES-Puro vector (Hanbio Biotechnology, Shanghai, China). To generate lentiviral vector overexpression of YB-1, the Open Reading Frame (ORF) of YB-1 was inserted to the MCS sites of pHBLV-CMV-IRES-Puro vector (Hanbio Biotechnology, Shanghai, China). The lentiviral vector driven *Hnscr* knockdown was generated by inserting the shRNA sequence target for *Hnscr* to pHBLV-U6-Puro vector (Hanbio Biotechnology, Shanghai, China). To generate lentiviruses, the lentiviral vectors and packaging vectors were co-transfected into 293FT cells.

Luciferase Activity and ChIP Assays

luciferase activity assays were performed in transiently transfected HEK293 cells, the firefly and Renilla luciferase activities were measured by a Dual-Glo Luciferase Assay System (Promega). For ChIP assay, chromatin extracted from *Hnscr* knockdown htNSCs, YB-1 knockdown htNSCs or control cells were precleared and immunoprecipitated by immunoglobulin G (IgG) or antibodies against YB-1 (Santa Cruz Biotechnology, sc-398146), respectively. The occupancy of YB-1 on the promoter region of $p16^{INK4A}$ was measured by qPR-PCR analysis.

RNA Pull-down Assay

RNA pull down assay was performed as described previously (Hu et al., 2014). Briefly, biotin-labeled full-length *Hnscr* or truncated *Hnscr* probes were incubated with nuclear lysate of htNSCs for 60 min. Then, streptavidin agarose beads (Invitrogen) were added and incubated at room temperature (RT) for another 60 min. After washed with ice-cold NT2 buffer, the retrieved proteins were subjected to mass spectrometry or western blot analysis.

RNA Immunoprecipitation

RIP assay was performed by a Magna RIP RNA-Binding Protein Immunoprecipitation Kit (Millipore, 17-700) according to manufacturer's instructions. The RNA samples precipited were extracted, reverse transcribed and subjected to qRT-PCR analysis.

RNA Sequencing and Bioinformatics Analysis

total cellular RNAs of htNSCs derived from young mice and aged mice or *Hnscr* null mice and WT mice were subjected to commercial RNA-seq (Annoroad Gene Tech. (Beijing) Co., Ltd). RNA-seq data were uniquely mapped to the reference genome with HISAT 2.0.5. Expression values at the gene level were assigned by HTSeq 0.6.0. Differently expressed genes were identified by DEGseq 1.18.0 and DESeq 1.16.0 on the basis of $p < 0.05$. Hierarchical clustering of gene expression changes was generated in Cluster 3.0 and visualized with JavaTree View. Heatmaps were generated to show the differences in gene expression of htNSCs derived from different groups of mice. GO Enrichment (fisher.test and p.adjust) was performed to show the biological processes affected among different groups of htNSCs.

Molecular Docking and Virtual Screening

molecular docking and virtual screening of natural small molecular compounds which may bind to YB-1 were performed under the help of Guangzhou Yinfo Information Technology Co. Ltd. Briefly, homology modeling of mouse YB-1 structure was performed by MODELER software based on the structure of human YB-1 (PDB code: 1H95). Structure with lowest energy was chosen for further structure refinements. To identify optimized conformations, loop refinement was applied to the predicted structure of mouse YB-1. The potential binding sites of YB-1 was predicted by the online tool POCASA 1.1. Molecular docking based virtual screening was conducted between YB-1 and the natural small molecular compounds library of Target Molecule (Target Mol) via AutoDock Vina and DOCK 6.7. Virtual screening parameters were prepared by autodock tools (ADT).

Western Blot and qRT-PCR

Western Blot and qRT-PCR analysis were performed as reported previously (Xiao et al., 2017). The western blot antibodies used in this study are: rabbit anti-YB-1 (9744), mouse anti-Ubiquitin (3936), rabbit anti-$p16^{INK4A}$ (92803) and rabbit anti-GAPDH (5174) (Cell Signaling Technology). Validation information is available on the manufacturers' websites. The qRT-PCR primers used in this study are listed in Table S6.

Micro-CT Analysis

Micro-CT analysis were performed as reported previously (Li et al., 2015; Yang et al., 2017). Femora were dissected from mice, fixed with 4% paraformaldehyde for 24 h and analyzed by high-resolution μCT (Skyscan 1172, Skyscan). The scanner was set at a voltage of 65 kV, a current of 154 μA and a resolution of 13.98 μm per pixel. The image reconstruction software (NRecon v1.6), data analysis software (CTAn v1.9) and three-dimensional model visualization software (μCTVol v2.0) were used to analyze the parameters of the distal femoral metaphyseal trabecular bone. We selected the region of interest (ROI) for analysis as 5% of femoral length below the growth plate. Trabecular bone volume per tissue volume (Tb. BV/TV) was measured.

QUANTIFICATION AND STATISTICAL ANALYSIS

All data are presented as means ± SEM. Statistical analysis was performed by unpaired two-tailed Student's t test, or one-way or two-way analysis of variance (ANOVA) followed by Bonferroni's post test, in GraphPad Prism 7.0. Kaplan–Meier survival analysis was performed by SPSS 20.0. $p < 0.05$ was considered to be statistically significant. The sample size for *in vivo* and *in vitro* experiments was based on previous experience. All the samples were randomly assigned and none of the experiments in the study were performed in a blinded fashion. For both *in vitro* and *in vivo* experiments, no initial exclusion criteria were used and no animals or replicates were excluded from the study.

DATA AND CODE AVAILABILITY

All the data that support the findings of this study are available from the corresponding author upon reasonable request. The accession number for RNA sequencing data reported in this paper is SRA: PRJNA505113.